Chinese Chemical Letters 34 (2023) 108280

Contents lists available at ScienceDirect

Chinese Chemical Letters

journal homepage: www.elsevier.com/locate/cclet

A review on hydrogen production from ammonia borane: Experimental and theoretical studies

Jinrong Huo[a,c], Kai Zhang[a,c], Haocong Wei[a,c], Ling Fu[e], Chenxu Zhao[c,d], Chaozheng He[c,d,*], Xincheng Hu[b,*]

[a] School of Sciences, Xi'an Technological University, Xi'an 710021, China
[b] Henan Engineering Center of New Energy Battery Materials, College of Chemistry and Chemical Engineering, Shangqiu Normal University, Shangqiu 476000, China
[c] School of Materials Science and Chemical Engineering, Institute of Environmental and Energy Catalysis, Xi'an Technological University, Xi'an 710021, China
[d] Shaanxi Key Laboratory of Optoelectronic Functional Materials and Devices, School of Materials Science and Chemical Engineering, Xi'an Technological University, Xi'an 710021, China
[e] College of Resources and Environmental Engineering, Tianshui Normal University, Tianshui 741001, China

ARTICLE INFO

Article history:
Received 20 December 2022
Revised 18 February 2023
Accepted 28 February 2023
Available online 3 March 2023

Keywords:
Ammonia borane
Hydrogen production
Dehydrogenation catalyst
Hydrolysis
Methanolysis
Photo-piezoelectric synergy

ABSTRACT

Ammonia borane (NH_3BH_3, AB) is an ideal raw material of hydrogen production with higher hydrogen storage capacity. In this paper, the catalytic processes of AB dehydrogenation were described from different ways, including thermal dehydrogenation, hydrolysis, methanolysis, photocatalysis and photo-piezoelectric synergy catalysis with experimental research and theoretical calculations. Catalyst models include bulk materials, two-dimensional materials, nanocluster particles and single/diatomic structures. Among them, the proportion of H_2 released is different, and the reaction conditions are also different, which are suitable for different application scenarios. Through this review, we could have a preliminary comprehensive understanding of AB dehydrogenation reaction.

1. Introduction

H_2 is a clean and renewable fuel. So it will play a vital role in transition from conventional fossil fuels to renewable energy sources on the way towards a sustainable energy future. Like H_2 production from ammonia borane, water splitting is also a promising startegy [1–3]. The safe storage and transportation of H_2 has become the most important challenge. Ammonia borane (AB), the simplest type of B–N hydride, with a molecular weight of only 30.7 g/mol and a hydrogen storage capacity of up to 19.6 wt%, which was successfully synthesized in 1955 by Shore and Parry [4]. Ammonia borane become the most promising hydrogen carrier materials because it has some excellent physical and chemical properties, such as remain stable solid form at ambient conditions, high hydrogen content, eco-friendly, and high solubility in most solvents. AB coulde released ultrapure hydrogen *via* dehydrogenation reaction, hydrolysis reaction and methanolysis reaction.

2. Synthesis of AB

In the 1950s, with the help of diethyl ether, Shore and Parry [4,5] synthesized AB through lithium borohydride and diammoniate of diborane. The reaction process is expressed as follows:

$$LiBH_4 + NH_4Cl\,or\,(NH_4)_2SO_4 \xrightarrow{\text{Diethylether}} LiCl\,or\,Li_2SO_4 + H_3NBH_3 + H_2 \tag{1}$$

$$[H_2B(NH_3)_2^+][BH_4^-] + NH_4Cl \xrightarrow{\text{Diethylether}} [H_2B(NH_3)_2^+][Cl^-] + H_3NBH_3 + H_2 \tag{2}$$

Yields of AB are only 45% of this process, which is far from enough for large-scale commerce applications of AB. Enhancing the yields of AB are one of the main goals. Heldebrant *et al.* [6] through metathesis of NH_4X and MBH_4 salts in liquid NH_3 to synthesize AB and it is synthesized efficiency reach 99%. The reaction process is as follows:

$$NH_4Cl + LiBH_4 \rightarrow NH_3BH_3 \tag{3}$$

---

[*] Corresponding authors.
E-mail addresses: hecz2019@xatu.edu.cn (C. He), huxincheng2019@163.com (X. Hu).

https://doi.org/10.1016/j.cclet.2023.108280

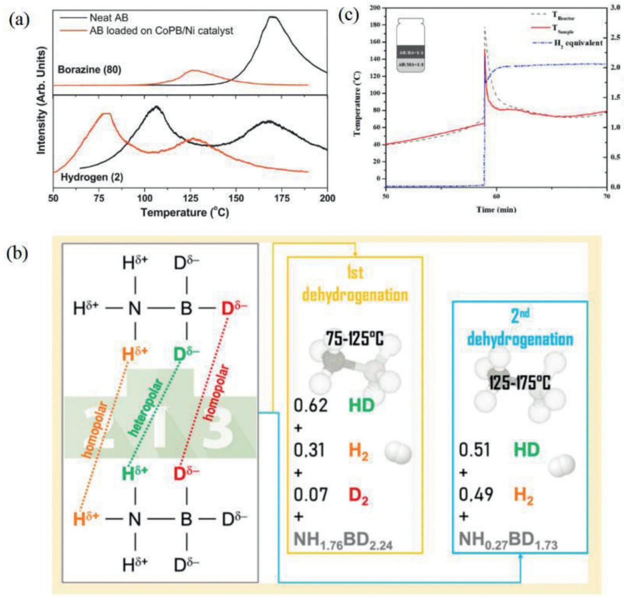

Fig. 1. (a) TPDS/MS profiles of neat AB powder and AB loaded over Co-P-B/Ni catalyst, by using THF based solution. The scanned temperature was between 50 °C and 200 °C at heating rate of 2 °C/min. The hydrogen and borazine with atomic mass of 2 and 80, respectively, have been highlighted in the figure. Copied with permission [12]. Copyright 2012, Elsevier. (b) The release of H_2 between 75 °C and 175 °C (covering the two-step dehydrogenation of AB). Copied with permission [14]. Copyright 2018, American Chemical Society. (c) Temperature and H_2 equivalent profiles for AB with two additives (bottom AB:MA = 1:1, top AB:BA = 1:1). MA: maleic acid ($C_4H_4O_4$). BA: boric acid. Copied with permission [15]. Copyright 2020, Elsevier.

So far, the high efficiency of AB has been achieved, which greatly promotes the wide application of AB.

Since 1995, the synthesis efficiency of aminoborane has increased from an initial 45% to 99% (prepared by the reaction of $NH_4X + MBH_4$ in liquid ammonia, where X represents halogen and M represents alkali metal). Ramachandran from Purdue University in the United States and his scientific research team have been committed to the study of the preparation reaction of aminoborane for many years. In 2015, they further optimized the reaction conditions, so that SBH ($NaBH_4$) and $(NH_4)_2SO_4$ could react to prepare aminoborane in an open environment in the presence of THF(C_4H_8O), and the reaction yield could reach more than 90%. This greatly reduces the price of commercial ammoniborane and improves the practicality of large-scale application of AB [7–9].

3. Thermal dehydrogenation of AB

One method of releasing hydrogen from AB is thermal dehydrogenation [5–7]. The process of thermal dehydrogenation of AB as follows (Fig. 1a):

$$H_3BNH_3 \rightarrow H_2BNH_2 + H_2 \uparrow H_2:\ 6.5\ \text{wt\%},\ 90-130\,^{\circ}C \tag{4}$$

$$H_2BNH_2 \rightarrow HBNH + H_2 \uparrow\ H_2:\ 13.0\ \text{wt\%},\ 130-150\,^{\circ}C \tag{5}$$

$$HBNH \rightarrow BN + H_2 \uparrow\ H_2:\ 19.6\ \text{wt\%},\ \geq 150\,^{\circ}C \tag{6}$$

This indicates that AB is stable at a lower temperature ($< 90\,^{\circ}C$), and the release of H_2 requires a higher temperature, which limits the applicable of AB. So, looking for a catalyst material that catalyzes the ammonia borane dehydrogenation reaction at room temperature or about room temperature has been a major challenge. Experimental and theoretical efforts have been made to achieve this goal.

3.1. Experimental research

In order to make full use of H_2, the dehydrogenation of ammonia borane should be realized in the near proton exchange membrane (PEM) fuel cell operating temperatures (–85 °C) [10,11]. Co-P-B coating on Ni (Fig. 1a) [12] and silicon nanoparticles [13] catalysts were used to study thermal decomposition of ammonia borane and can achieve the maximum hydrogen production rate at around 80 °C. At the same time, for safety, we should ensure that the mixture of AB and catalyst is stable below 50 °C and does not produce H_2. Therefore, it is very important to raise the triggering temperature of catalyst to about 60 °C. By heating NH_3BD_3 to about 200 °C until two H_2 molecules are released, hydrogen (HD) was released mainly from heteropolar hydrogen-deuterium interactions ($N{-}H^{\delta+}\cdots{}^{\delta+}D{-}B$) and homopolar dihydrogen interactions ($N{-}H^{\delta+}\cdots{}^{\delta+}H{-}N$), and homopolar dideuterium interactions ($B{-}D^{\delta-}\cdots{}^{\delta-}D{-}B$) is negligible (Fig. 1b) [14]. As shown in Fig. 1c [15], using this configuration, a mixture of AB:MA = 1:1 was placed at the bottom, while another mixture of AB:BA = 1:1 was added at the top, the H_2 equivalent was improved to 2.11 at 60 °C. This also increases the H_2 yield and lowers the temperature required for the reaction.

Cu metal has better catalytic activity for AB thermal catalytic process. As shown in Figs. 2a and b, the study have shown that $CuCl_2$ has the highest catalytic activity at 85 °C among $FeCl_2$, $CoCl_2$, $NiCl_2$, $CuCl_2$, and $ZnCl_2$ [16]. Moreover, Salinas-Torres *et al.* [17] added Cu atom in $La_{0.7}Sr_{0.3}CoO_3$ and realized the highest catalytic activity among, when containing 2.72 wt% of Cu, turnover frequency (TOF) reaches 843 L H_2/h. In this process, the closer interaction Cu-Co might be favoring the catalytic activity. The catalytic process is shown in Fig. 2c.

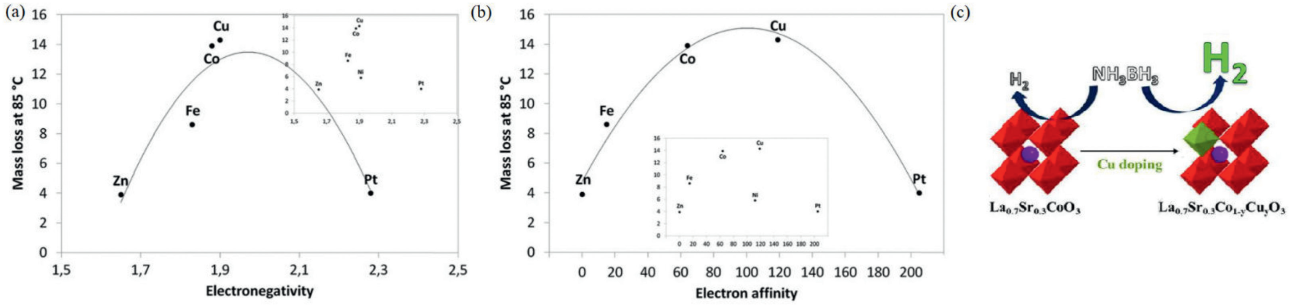

Fig. 2. Mass losses at 85 °C as a function of (a) the electronegativity and (b) the electron affinity of M (*i.e.*, Fe, Co, Cu, Zn and Pt) of MCl_2 (Insets showed the plots when Ni is taken into consideration). Copied with permission [16]. Copyright 2012, Elsevier. (c) Schematic diagram of AB dehydrogenation catalyzed by Cu-doped La-Sr-Co-O compound. Copied with permission [17]. Copyright 2019, Elsevier.

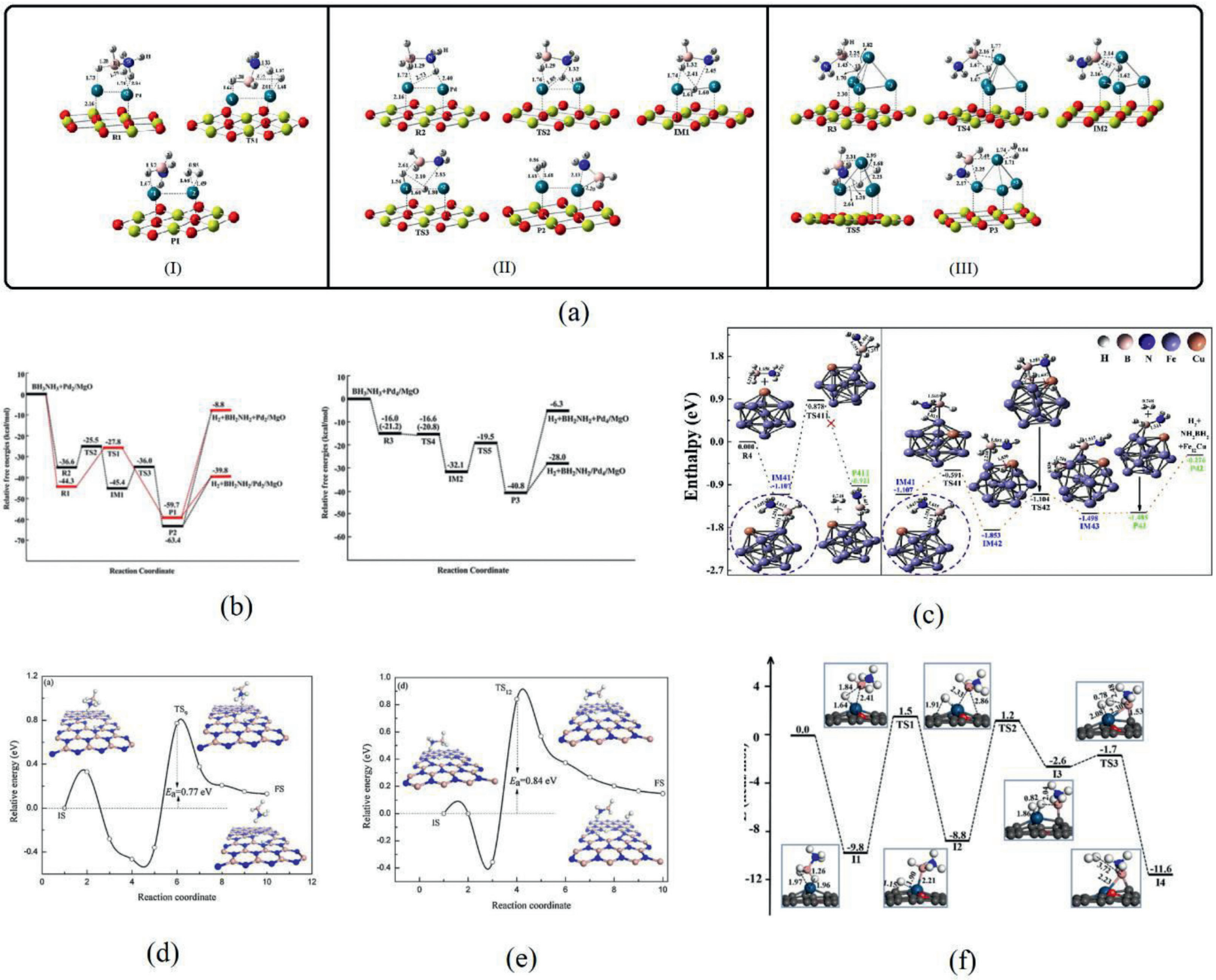

Fig. 3. (a) Optimized structures on the Pd_2/MgO(100) and Pd_4/MgO(100)surface for the stepwise dehydrogenation pathway. Copied with permission [18]. Copyright 2013, Elsevier. (b) Schematic Gibbs free energy profiles for the concerted and stepwise dehydrogenation pathways: on the Pd_2/MgO surface and on the Pd_4/MgO surface. Copied with permission [18]. Copyright 2013, Elsevier. (c) The reaction pathways for the dehydrogenation reactions between $Fe_{12}Cu$ dimer and AB molecule. Copied with permission [19]. Copyright 2016, Elsevier. (d, e) Energetic profiles for the reaction between AB and defective h-BN sheets. Copied with permission [20]. Copyright 2016, Elsevier. (f) The relative energy profiles of the releasing of the first hydrogen molecule from NH_3BH_3 catalyzed by Pt_1/Gr-O. Copied with permission [21]. Copyright 2018, Chinese Physical Society.

3.2. Theoretical calculations

Tong *et al.* [18] construct two catalyst structures of AB-Pd_2/MgO and AB-Pd_4/MgO to investigated dehydrogenation mechanism of ammonia borane by DFT/UB3LYP method (Fig. 3a). The calculation results are shown in Fig. 3a and rate determining step (RDS) barrier reach 9.4 and 12.6 kcal/mol, respectively (Fig. 3b). Zhou *et al.* [19] calculated the catalysts of Fe_2, FeCu, and $Fe_{12}Cu$ to catalyze dehydrogenation of AB through Gaussian 03 Program and for $Fe_{12}Cu$ catalyst, overall exothermic and barrierless were achieved, as shown in Fig. 3c. Kuang *et al.* [20] calculated various possible paths that pristine and defective h-BN sheets catalyst material catalyzed the dehydrogenation of AB to H_2, indicating that defective was conducive to improving the catalytic activity. The defective h-BN sheets with VB and V_3B+N vacancies are excellent metal-free catalysts for facilitating the hydrogen release of AB [20]. As shown in Figs. 3d and e, the energy barriers to release the H_2 are 0.77 and 0.84 eV, respectively. This is a lower activation barrier than N-doped graphene catalysts. Wu *et al.* [21] showed that single Pt atoms supported on oxidized graphene (Pt_1/Gr-O) catalyst can catalyze AB hydrolysis. The rate-limiting barrier is 16.1 kcal/mol, and the catalyst can spontaneously recover after H_2 release. The production process of the first H_2 molecule is shown in Fig. 3f. Based on the Kissinger method and isoconversional model-free fitting method of AB, and solid-state kinetics model-based method, Gangal and Sharma [22] obtained a new mechanism, based on the fundamental kinetic equations and isothermal experimental data.

We focus on the thermal decomposition of AB catalyzed by two-dimensional (2D) materials or nanoclusters (Fig. 4). Using 2D $MgSiP_2$ structure [23] as the catalyst, we achieved the dissociation of 6 H atoms in AB, and 1 mol AB could generate 3 mol H_2 without the participation of H_2O molecules in the reaction. AB dehydrogenation is realized on the surface of Os/P_3C monatomic structure [24] catalyst, and the calculation shows that the doping of O atom can greatly reduce the activation barrier. The reaction process of AB thermolysis dehydrogenation was simulated by $Fe_{22}@Co_{58}$ core-shell structure and $Fe_{36}Co_{44}$ bimetallic nanocluster catalyst [25,26].

4. Hydrolysis and methanolysis of AB

4.1. Hydrolysis of AB

The hydrolysis of AB is one of the safe and stable methods to prepare H_2. The hydrolysis reaction path with break of B-N bond

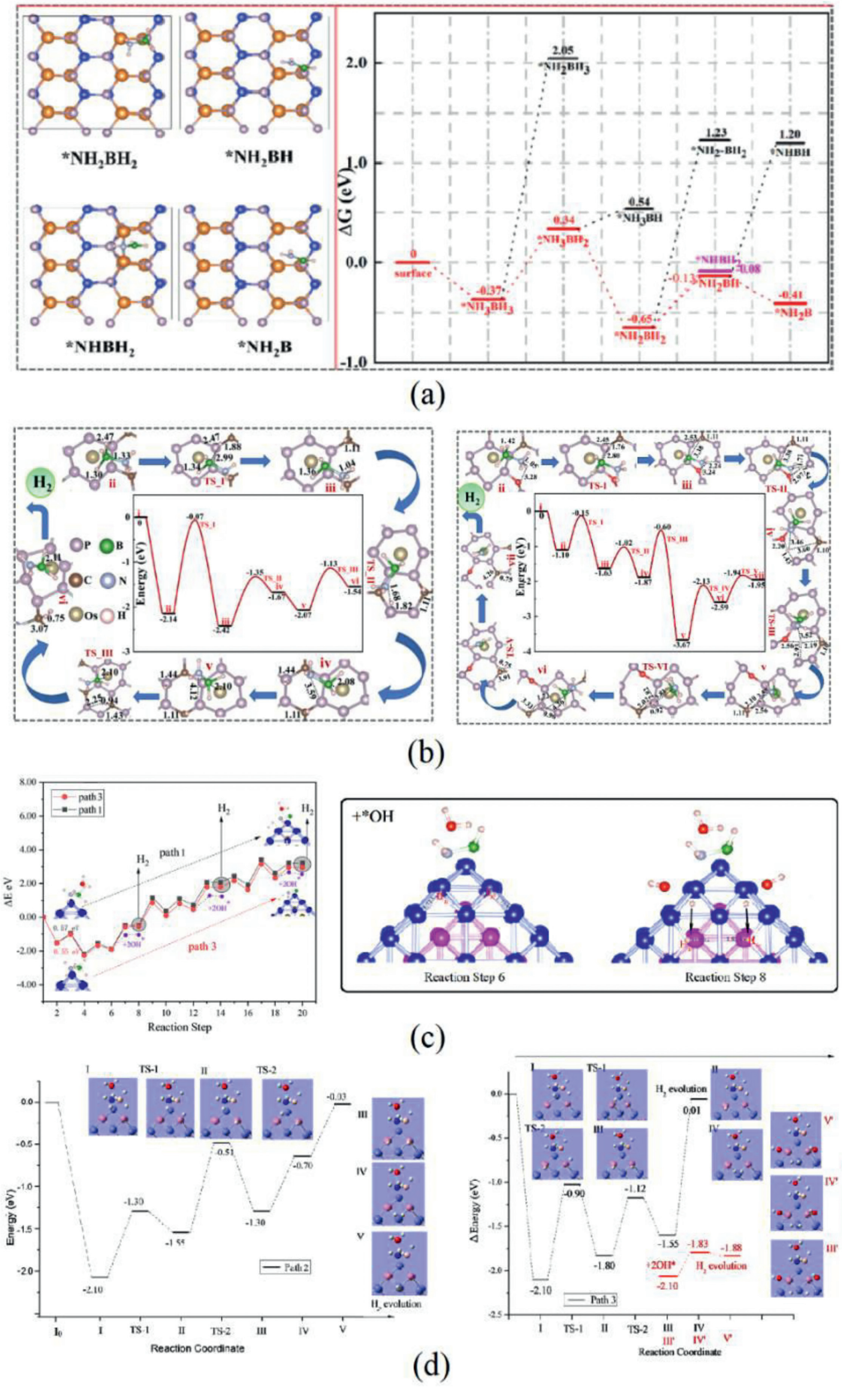

Fig. 4. (a) The structure of adsorbed intermediate states on the 2D $MgSiP_2$ structure and Gibbs free energy on the BN alternating dehydrogenation. Copied with permission [23]. Copyright 2022, Elsevier. (b) The complete free energy (ΔG) correction diagram and related structure diagrams for the dehydrogenation of AB molecules on the surface of Os/P_3C and Os/P_3C_O. Copied with permission [24]. Copyright 2022, Elsevier. (c) $Fe_{22}@Co_{58}$ core-shell structure and (d) $Fe_{36}Co_{44}$ bimetallic nanoclusters catalyzed dehydrogenation of AB by thermal decomposition. Copied with permission [25,26]. Copyright 2022, Elsevier.

can be divided into four types (Eqs. 7–10) [25,27,28]. There is no difference in the formation process of the first H_2, and the difference mainly comes from the formation of the second and three H_2, as shown in the following formula:

$$NH_3BH_3+4H_2O \rightarrow NH_4^+ + B(OH)_4^- + 3H_2 \uparrow \tag{7}$$

$$NH_3BH_3+2H_2O \rightarrow NH_4^+ + BO_2^- + 3H_2 \uparrow \tag{8}$$

$$NH_3BH_3+3H_2O \rightarrow NH_3B(HO)_3 + 3H_2 \uparrow \tag{9}$$

$$NH_3BH_3+3H_2O \rightarrow 2OH^- + NH_2^- + [BH(OH)]^{3+} + 3H_2 \uparrow \tag{10}$$

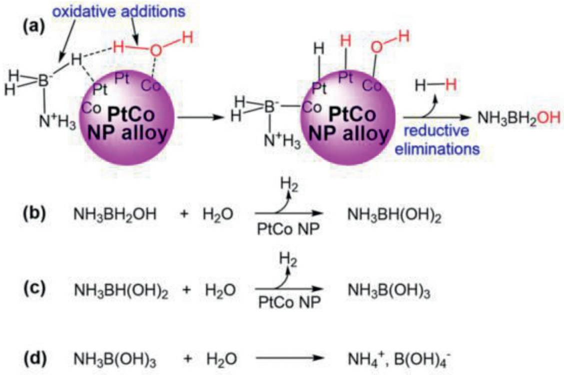

Scheme 1. (a–d) The possible mechanism for the AB dehydrogenation reaction on PtCo NP alloy.

In the other case that the B-N bond is not broken, the first H_2 molecule is produced as follows [29]:

$$NH_3BH_3+H_2O \rightarrow NH_3BH_2OH+H_2\uparrow \quad (11)$$

Taking Pt_1Co_1 as an example, the possible mechanism for the AB dehydrogenation reaction [30] is shown in Scheme 1.

4.1.1. Experimental research

Hydrolysis reaction is an effective catalytic process of AB dehydrogenation, and a variety of catalyst materials can show excellent catalytic activity (Table 1) [27–67]. Among them, $Ru_{0.5}Ni_{0.5}/g\text{-}C_3N_4$ catalyst has the lowest activation barrier energy (E_a), reaching 14.1 kJ/mol. It can be found that the presence of noble metal Ru can greatly improve the reactivity of the catalyst and the reaction rate. The RuP@NHMCs catalyst has the largest TOF of 4307 mL mol_{catal}^{-1} min^{-1} in the presence of 0.2 mol/L NaOH. This enhancement effect confirms that NaOH can behave as the catalyst promoter to facilitate the hydrolysis of AB at room temperature.

From Table 1, it can be seen that element P plays an important role in the catalytic process. The comparison of catalytic TOF of CoNiP/GO and NiCo-NC shows that the catalytic rate is increased by nearly 4 times. With the addition of P element, the catalytic activity barrier of CoP nanoparticles and Co/C is decrease significantly. In addition, the transition metal Ni also has a good catalytic activity. Comparing $Ru_{0.5}Ni_{0.5}/g\text{-}C_3N_4$ and Ru/CS, it can be found that due to the addition of Ni, the reactivity activation barrier becomes 1/3 of the previous one. Therefore, non-metals and transition metals also play an important role in the design of catalysts.

4.1.2. Theoretical calculations

Theoretical simulation can describe the structure and energy change of the reaction process more specifically. From the perspective of computational simulation, Peng and co-workers [27] described the formation process of the first H_2 molecule in detail with Ni_2P-catalyzed, as shown in Fig. 5. The remaining two H_2 molecules are formed by dropping the H atom which attached to B atom. The step-by-step reaction process can be expressed as follows (Eqs. 12–15):

$$NH_3BH_3+H_2O \rightarrow NH_4BH_3(OH) \quad (12)$$

$$NH_4BH_3(OH)+H_2O \rightarrow NH_4BH_2(OH)_2+H_2\uparrow \quad (13)$$

$$NH_4BH_2(OH)_2+H_2O \rightarrow NH_4B(OH)_3+H_2\uparrow \quad (14)$$

$$NH_4B(OH)_3+H_2O \rightarrow NH_4^+ + B(OH)_4^- + H_2\uparrow \quad (15)$$

Table 1
Activities of catalysts in the hydrolysis of AB at room temperature.

Catalyst	TOF (mL mol_{catal}^{-1} min^{-1})	E_a (kJ/mol)	Ref.
Hcp-CuNi/C	22.64	29.92	[39]
CoNiP/GO	134.6	44.12	[38]
NiCo-NC	35.2	43.6	[37]
Ru_1Co_9/TiO_2	1408	33.25	[36]
$Cu_{0.4}Co_{0.6}Pt_{0.0075}O$/RGO	854.0	39.8	[35]
CoP-CoO/NCDs	89.56	41.0	[34]
ZIF-67@Co	112.3	25.68	[33]
Pt/PAN(92)-co-P2EHA(8)	122.3	22.7	[32]
Rh/OPNC	1201	26.4	[31]
RuP@NHMCs	4307	36.3	[47]
Ru/CS	331.8	41.3	[46]
Ru-Cu alloy	626	26.3	[45]
$Ru_1Ni_{1.90}$/NCS	1017	26.5	[44]
$CuMoO_4$-$CoMoO_4$	104.7	38.4	[43]
$Pt^0/CoFe_2O_4$ nanoparticles	3628	65±2	[42]
Co-Cr-B	/	22.3	[41]
RuP_2/CDs	/	43.95	[40]
TiN−Pt Nanohybrids	346	29.2	[48]
CoRh@PVP	154	42.7	[67]
$Ni_{0.8}Pt_{0.2}$/GO	214.28	23.94	[66]
$Co_{0.8}Pt_{0.2}$/GO	230.76	23.60	[66]
$Ru_{0.5}Ni_{0.5}/g\text{-}C_3N_4$	840.3	14.1	[65]
$Ru_{0.85}Pd_{0.15}/g\text{-}C_3N_4$	948.2	24.2	[64]
$Pt_{76}Au_{12}Co_{12}$ nanoalloy	450	18.47	[63]
Pt/CNT-5W	710.1	27.8	[62]
Pt/CNT-10W	558	28.7	[62]
Rh^0/Co_3O_4	1800	61.7	[61]
$Ni_{0.8}Co_{1.2}P$@h-BN	86.5	40.26	[60]
$Pt_{0.5}Ni_{0.5}/g\text{-}C_3N_4$	250.8	38.09	[59]
$Cu_{0.4}Co_{0.6}$/BN nanofibers	8.42	21.8	[58]
Co-Mo-B	/	45.5	[57]
Ni/Ni_2P	68.3	44.99	[56]
Hnp-$Pt_{35}Cu_{65}$	108	40.5	[55]
Pt_1Co_1	476.2	28.8	[30]
Ni_2Pt@ZiF-8	600	23.3	[54]
$Co_{0.50}Cu_{0.50}$/NPs	/	38.12	[53]
CoP NA/Ti	42.8	34.1	[52]
1/1000Pt+Ni/CTF	12000	17.0	[29]
$Ni_{0.7}Co_{1.3}P$	58.4	43.2	[28]
CoP nanoparticles	72.2	46.7	[51]
Ni_2P	40.4	44.6	[27]
$Co_{35}Pd_{65}$ NPs	22.7	27.5	[50]
Co/C	/	62	[49]

The total reaction can be expressed as Eq. 16, and the whole reaction requires the participation of 4 H_2O molecules. After crossing the barrier of 0.12 eV (due to the binding of AB with the active atom of the catalyst), the whole reaction can occur spontaneously at room temperature.

$$NH_3BH_3 + 4H_2O \rightarrow NH_4^+ + B(OH)_4^- + 3H_2\uparrow \quad (16)$$

The break of the B-N bond in AB can also be achieved by OH^- attack, which is known as the S_N2 reaction mechanism. Hou *et al.* [28] simulated the formation of the first H_2 molecule by S_N2 reaction mechanism on $Ni_3P_2(0001)$ and $NiCo_2P_2(0001)$ surface catalysts.

As shown in Fig. 6, among the catalyst structures of Pt_1/Co_3O_4, Pt_1/CeO_2, Pt_1/ZrO_2, and Pt_1/ graphene, Pt_1/Co_3O_4 has the largest TOF (1220 min^{-1}) and the smallest E_a (37.4 kJ/mol) [68] and Pt_1/Co_3O_4 still maintained good catalytic activity after 15 cycles. As shown in Fig. 6e, after the adsorption of AB by Pt_1/Co_3O_4, the 5d electron of Pt atom interacts strongly with H atom, resulting in obvious elongation of B-H bond.

Using non-noble metal Fe and Co elements as main components, we completed the calculation of the catalytic hydrolysis reaction of AB catalyzed by $Fe_{36}Co_{44}$ bimetallic nanoclusters [26]. The path diagram is shown in Figs. 7a and b. Meanwhile, the different catalytic effects of different activation and coordination environments were analyzed in this work. We have completed the

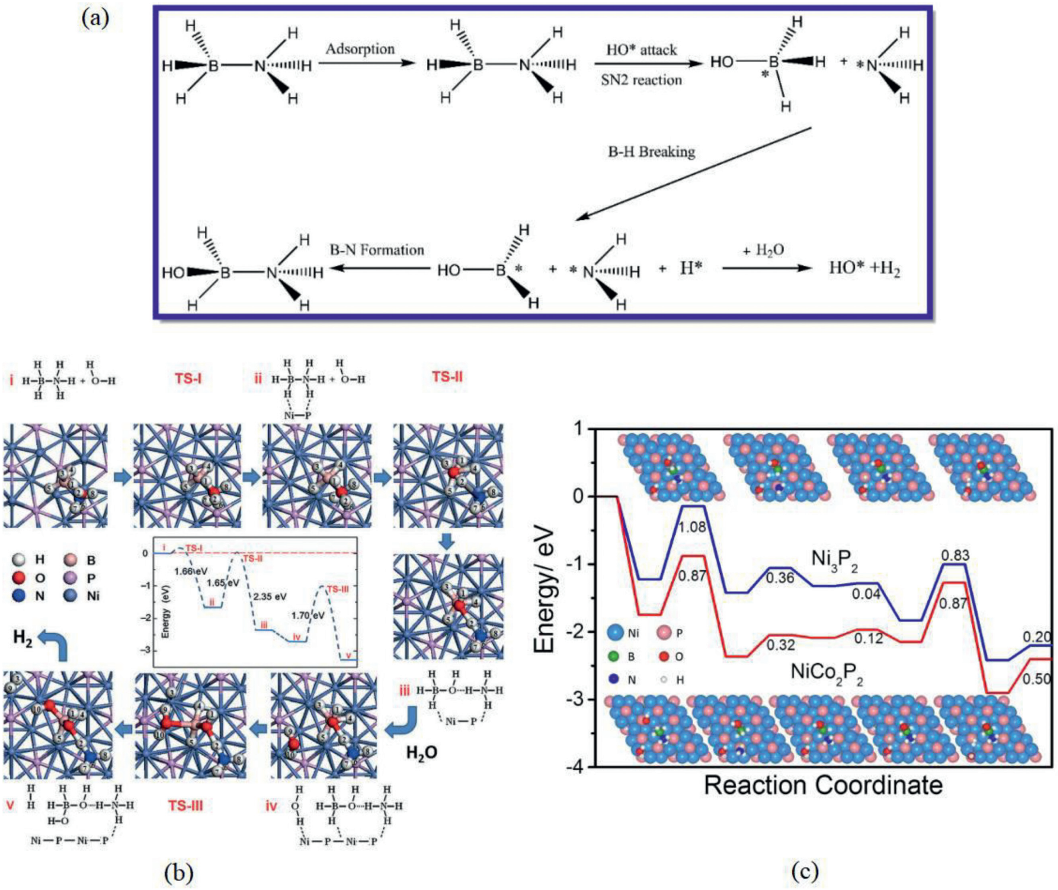

Fig. 5. (a) S_N2 reaction mechanism of AB dehydrogenation process. Copied with permission [28]. Copyright 2017, the Royal Society of Chemistry. (b) Plot of energy changes *versus* reaction coordinate calculated for Ni_2P-catalyzed hydrolysis of AB. Copied with permission [27]. Copyright 2015, Wiley. (c) Calculation of AB hydrolysis reaction catalyzed by $NiCo_2P_2$ and Ni_3P_2. Copied with permission [28]. Copyright 2017, the Royal Society of Chemistry.

complete calculation process of AB hydrolysis to prepare 3 mol H_2 using $Fe_{22}@Co_{58}$ core-shell as catalyst material (Fig. 7c), and it was found that there were new reaction paths (Eq. 17) beyond the paths shown in Eq. 16 (Fig. 5c) [25].

$$H_3NBH_3 + 2H_2O \rightarrow NH_4^+ + BO_2^- + 3H_2 \uparrow \tag{17}$$

In the case that the B-N bond is not broken, Li *et al.* [29] gave the catalytic reaction process on the Pt/Ni surface catalyst from the perspective of calculation simulation (Fig. 8a). From the calculation, it can be found that the incorporation of Pt atom reduces the reaction rate-determination step activation barrier (0.75 *vs.* 0.88 eV). Wu and co-workers [34] calculated the first H_2 formation process of Co(111), CoO(200), and CoO/CoP surfaces respectively from the perspective of calculation. And the high activity of CoP-CoO/surfaces was revealed (Fig. 8b). On the doped Ni(0001) surface, the rate-determining step of the AB hydrolysis reaction is the dissociation of H_2O molecule. Therefore, by means of the first-principles calculation, Li *et al.* studied the dissociation process of H_2O molecule [39] and the reaction path shown in Fig. 8c.

Therefore, the specific path of AB hydrolysis reaction is different for different catalysts, and this process needs to be further studied.

4.2. Methanolysis of AB

Liberation of NH_3 and inefficacy in recycling the hydrolysis product, metaborate become the mianly problems for hydrolysis of AB. Using methanol instead of water is a better choice, since that Ammonia borane has high solubility in methanol (23 wt% at 23 °C), methanolysis produces pure H_2 gas with no ammonia contamination, and the methanolysis product, ammonium tetramethoxyborate, is recyclable. The technology of ammonia borane methanolysis is another prominent technology that suitable for application in on-board hydrogen production. The methanolysis product of $NH_4B(OCH_3)_4$ can be converted back to AB by reaction with $LiAlH_4$ in the presence of NH_4Cl [69–72]. The process of Methanolysis of AB is shown in Eq. 18:

$$NH_3BH_3 + 4CH_3OH \xrightarrow{\text{Catalyst}} NH_4B(OCH_3)_4 + 3H_2 \uparrow \tag{18}$$

Methanolysis of AB occurs only in the presence of a suitable catalyst. Various catalytic systems consisting of homogeneous and heterogeneous metal catalysts, such as metal cations, monometallic nanoparticles (NPs), alloys, and core-shell catalysts have been studied for catalytic AB methanolysis. Among them, noble metal catalysts such as Pd [70,73–75], Pt [76], Ru [77–81], Rh [82–89] and Cu [90–92] nanoparticles have been determined to have superior catalytic activities for H_2 release from AB methanolysis. The results are shown in Table 2. Ru/Immobilized in Montmorillonite catalyst had the lowest activation barrier, indicating that the noble metal has good catalytic activity. However, their high cost and less content hinder their widespread use for practical applications. Therefore, development of cost-saver, efficient, and reusable supported catalysts is very vital to overcome aforementioned problems for on-board applications. So far, there are few reports on computational simulation of methanolysis reaction, which needs to be supplemented by researchers in subsequent studies.

As shown in Table 2, TOF and E_a of methanolysis of AB are listed. It can be found that Ru/MMT [77] has the lowest E_a, indicating that noble metal catalyst has high catalytic activity. CuNi NPs

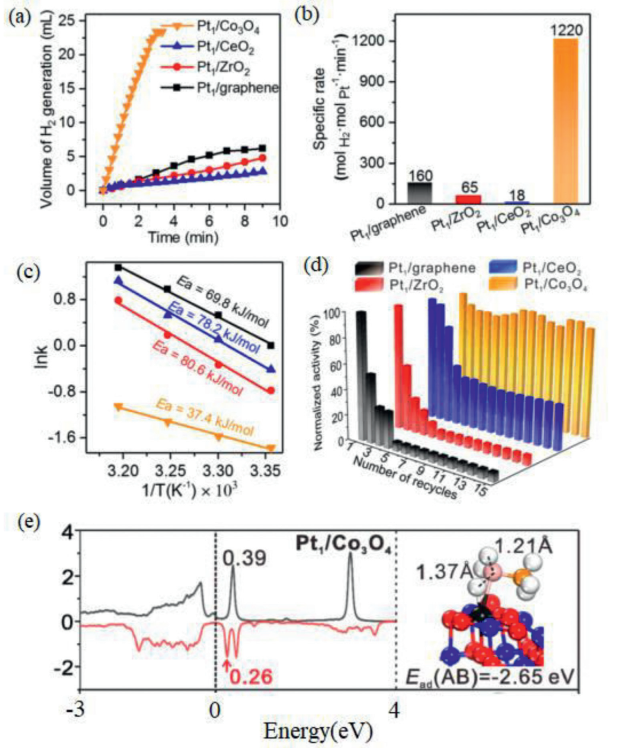

Fig. 6. (a–d) Catalytic performance of Pt_1 SACs in hydrolytic dehydrogenation of AB at 25 °C. (e) Local partial density of state (LPDOS) projected of Pt_1/Co_3O_4 on the Pt_1 5d orbitals with the Fermi level set at zero and the local configurations for AB adsorption. Copied with permission [68]. Copyright 2019, American Chemical Society.

Table 2
Activities of catalysts in the methanolysis of AB at room temperature.

Catalyst	TOF (min^{-1})	E_a (kJ/mol)	Ref.
Pd(0) nanoparticles	101.58	46	[70]
Pd NCs	22.3	35	[73]
CoPd/C	27.7	25.5	[74]
$Ag_{30}Pd_{70}$/C	366.4	37.5	[75]
Pt nanoparticles	283	-	[76]
Ru/MMT	29	23.8 ± 1.2	[77]
Ru NPs@nano-CeO_2	27.37	111.14	[78]
PVP-stabilized Ru(0) nanoclusters	47.6	58 ± 2	[79]
Graphene supported ultrafine Ru(0) NPs	24.4±0.5	54.1 ± 2	[80]
Ru NPs@PCC-2	304.4	-	[81]
Ru NPs@PVP	38.1	-	[81]
Zeolite confined Rh(0) nanoclusters	385	40 ± 2	[82]
Nanoceria supported Rh(0) nanoparticles	144	64.6 ± 2.0	[83]
L-Proline-functionalized Rh nanoparticles	1035	38.2	[84]
$Rh_{51}Co_{49}$@HA nanoclusters	193.7	52.7	[85]
$Rh_{26}Cu_{74}$@HA nanoclusters	25.1	59.7	[85]
$Rh_{45}Fe_{55}$@HA nanoclusters	38.7	54.1	[85]
Rh(0)/nanoHAP	147	56 ± 2	[86]
Rhodium(0) nanoparticles supported on nanosilica	168	62 ± 2	[87]
Nanoalumina-supported Rh (0) nanoparticles	218	62 ± 2	[88]
Rh/CC3-R-homo	215.3	-	[89]
Cu nanostructures	2.41	34.2 ± 1.2	[90]
Supported copper-copper oxide nanoparticles	24	69.7	[91]
CuNi NPs	49.1	24.4	[92]

[92] also has a low E_a, indicating that transition metal elements also can serve as a good methanolysis of AB catalyst.

5. Photocatalysis

Photocatalysis is a clean reaction process. It is an important research direction to realize the dehydrogenation process of AB under visible light ($\lambda > 420$ nm) by reducing the band gap of semiconductor catalyst.

5.1. Experimental research

Visible light is the most abundant and convenient clean energy, which is constantly available and very easy to obtain. Therefore, visible light catalysis is an important research direction. For example, Au and Ag [93] are excellent photocatalytic materials with excellent LSPR in the ultraviolet and near-infrared regions. Au nanoparticles deposited on TiO_2 [94] catalysts can be used as electron traps to prevent electron-hole recombination, thus improving catalytic activity.

Oxides are often important photocatalytic materials. under visible light irradiation ($\lambda > 420$ nm), MoO_{3-x} [95,96] and WO_{3-x} nanowires [97] could catalyze ammonia borane to generate H_2 (Figs. 9a and c), which opens up new prospects for efficient heterogeneous catalysis of plasma semiconductor nanostructures. Through the load of the noble metal Rh, the activity of Rh/WO_{3-x} [98] catalysts were further improved with a TOF as high as 805.0 mol_{H2} $mol_{Rh}{}^{-1}$ min^{-1} and an apparent activation energy of 45.2 kJ/mol (Fig. 9b).

As shown in Fig. 10, in Pd/$H_2Ti_3O_7$ composite nanowires catalyst [99], excited electrons accumulate to Pd under light conditions, so the existence of Pd promotes the separation of electron-hole and prevents electron-hole recombination. This synergy enhanced the catalytic activity of Pd/$H_2Ti_3O_7$ composite nanowires. Monometallic Co and bimetallic CuCo and FeCo catalysts supported by g-C_3N_4 are catalysts for transition metal nanoclusters [100]. After electrons are activated in g-C_3N_4 under light, they transfer to metal atoms. The metal atom becomes the center of catalytic activity. Taking CoAu/g-C_3N_4 catalyst [101] as an example, under the influence of the Mott-Schottky effect, electrons are transferred from the conduction band of g-C_3N_4 to metal and a potential barrier is formed to prevent electron countercurrent. Under the influence of light, more electrons are excited into the metal, increasing the separation of charge.

With favorable transfer properties, better dispersion, CdS-TiO_2/carbon nanocomposite with high surface area [102] has become a good catalyst for ammonia borane dehydrogenation. Using non-noble metal nanoparticle supported on a chromium-based MOF (MIL-101) [103], such as Cu/MIL-101, can efficient catalysts H_2 production in the hydrolysis of AB. The electrons generated by illumination concentrate on the surface of Cu atoms, making Cu atom become a good reduction catalytic site, and MIL-101 becomes a good oxidation active site. Co and Ni NPs supported by these C_3N_4 species [104], where TOF of Co/C_3N_4 reaches 93.8 min^{-1}, which exceeded the values of all the reported heterogeneous noble metal-free catalysts, has excellent catalytic activity. Co and Ni NPs supported by seven photoactive and non-photoactive MOFs [105], Co-based catalysts had the highest activities among the reported noble-metal-free catalysts at 298 K. The TOF value is 117.7 min^{-1} and the activity almost as good as that of noble metal catalyst.

Under light conditions, NiCu alloy loaded carbon nitride nanosheets (Ni_xCu_y/CNS) [106] realized the hydrolysis process of AB (Figs. 11a and b). Under the effect of localized surface plasmon resonance (LSPR), charge accumulates from Cu to Ni, and the catalytic reaction with Ni as the active site achieves the break of B-H bond in AB and O-H bond in H_2O. In Au-Co nanoparticles (Au-Co@CN), electrons flow from g-C_3N_4 and Co atoms to Au atoms, and thus Au act as active atoms (Figs. 11a and b). For Co/$P_{3.59}$CN nanocluster catalyst [107], electrons accumulate towards Co atoms, which makes Co atoms behave more like noble metals with higher activity (Figs. 11c and d). At 298 K, TOF reaches to 67.09 $mL_{H_2}{}^{-1}$ $min_{Co}{}^{-1}$. The comparison between Ru/g-C_3N_4 and Ru/C/g-C_3N_4 shows that [108], when Ru/C(1.0)/g-C_3N_4,

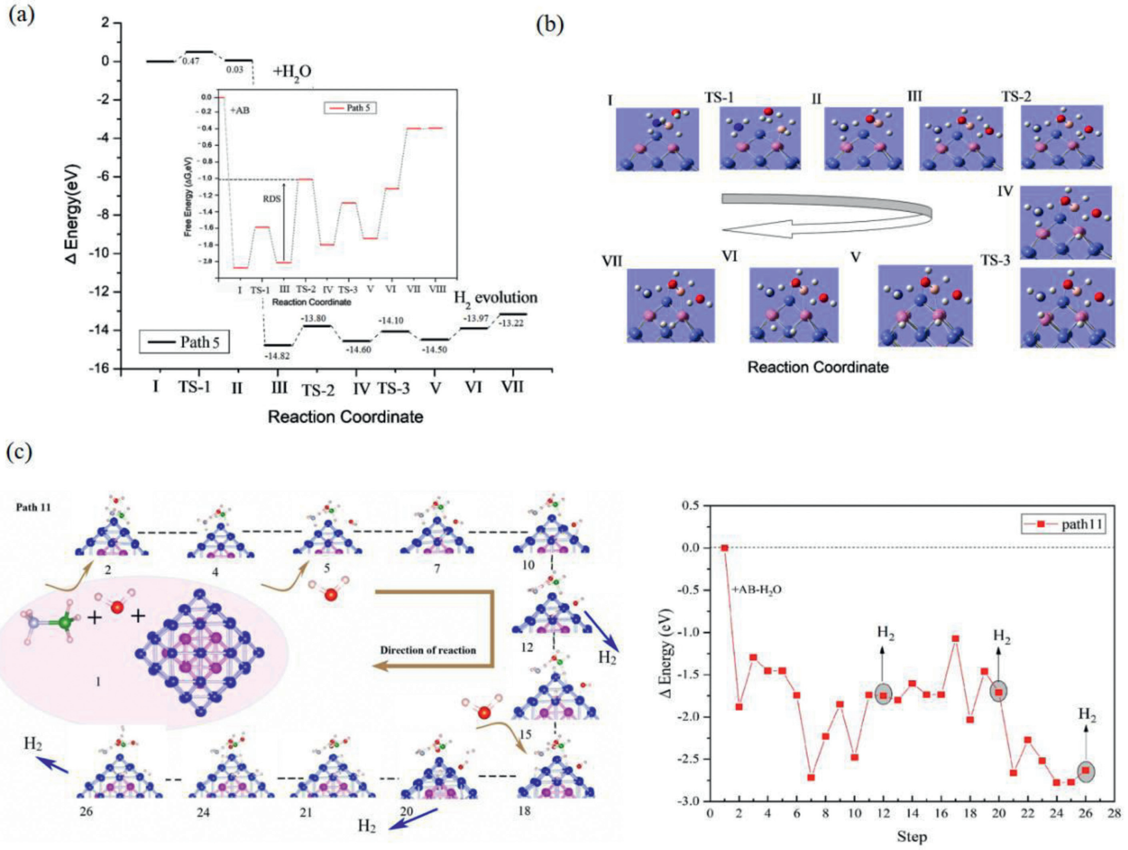

Fig. 7. (a, b) Reaction paths of $Fe_{36}Co_{44}$ Bimetallic nanoclusters catalyzed AB hydrolysis. Copied with permission [26]. Copyright 2022, Elsevier. (c) $Fe_{22}@Co_{58}$ core-shell catalytic hydrolysis of AB to prepare 3 mol H_2. Copied with permission [25]. Copyright 2021, Elsevier.

average Ru NP size is the smallest, and the maximum TOF reaches 196.4 h^{-1}. The TOF of RuP_2-/g-C_3N_4 [109] could reach 175 min^{-1} under light conditions (Fig. 11e). At the same time, the change of P atom ratio will greatly affect Schottky barriers and promote electron movement (Figs. 11c and d). Oxide based Co/V_2O_5 [110] and Ti_2O_3 [111] have a narrow band gap, which can realize the catalytic process of ammonia borane dehydrogenation under light conditions. In Co/V_2O_5, photogenerated electrons transfer from V_2O_5 to Co atoms. It is an important research direction to realize AB dehydrogenation at low temperature. Through a reduction transformation method, nanoscale Ti_2O_3 particles with high chemical stability and narrow band gap are prepared, realizing a rapid production of 2.0 equiv. of hydrogen from AB at ambient temperature (Fig. 12a) [105,111]. In NiCoP/TiO_2 [112] catalyst, under visible light NiCoP work as sensitizer to absorb light and generate electron-hole pair while TiO_2 work as electron trapper. So positively charged NiCoP surface and negatively charged TiO_2 surface are achieved under visible light, and the H_2 generation rate from hydrolysis of AB was increased to 2.0 folds, with E_a reduced from 52.76 kJ/mol to 25.89 kJ/mol. However, if 2.5%Pt is added to TiO_2, the reaction rate will increase to 0.55 mL/s (Fig. 12b). In different proportions of CuNi/TiO_2-CdS, $Cu_{0.45}Ni_{0.55}$/TiO_2-CdS catalyst [113] had the fastest hydrogen evolution rate with a high conversion frequency (TOF) of 25.9 mol_{H_2} $mol_{cat}{}^{-1}$ min^{-1} at 25 °C and low activation energy of 32.8 kJ/mol (Fig. 12c). The band gap of TiO_2 structure modified by Fe^{3+} and graphene decreases [108,114], and the light absorption spectrum line has an obvious red shift (Fig. 12d). When added graphene concentration is 1% and Fe^{3+} concentration is 2%, H_2 production efficiency is the highest, reaching 1235.32 μmol min^{-1} $g_{cat}{}^{-1}$ (Fig. 11d).

Au-Ru alloy [115] and Ag@Pd core-shell nanocubes [116] catalysts show significant light-boosting effect. Among them, the TOF of Au-Ru alloy catalyst reaches 240 mol_{H_2} $mol_{cat}{}^{-1}$ min^{-1}. Under the influence of light, electron transfer can be realized. For example, in Co-$CeVO_4$/CeO_2 catalyst [117], electrons are transferred from CeO_2 to $CeVO_4$ and then to Co atoms, thus forming electron-hole centers, respectively (Fig. 13).

5.2. Theoretical calculations

TiN-Pt nanohybrid can catalyze the dehydrogenation of AB under light conditions [48]. The calculated study shows that the barrier of H_2O dissociation in AB hydrolysis reaction is 0.3 and 0.5 eV under illumination and no illumination, respectively (Fig. 14a), indicating that illumination reduces the activation barrier.

Theoretical calculations show that the addition of Cu atoms greatly reduces the dissociation barrier of H_2O, which is the RDS of AB hydrolysis, and the migration barrier of OH, which enables the reaction process to be carried out at lower temperatures. NiCu alloy loaded carbon nitride nanosheets (Ni_xCu_y/CNS) catalyst [106], under the influence of LSPR, electrons are transferred from Cu to Ni atoms, which makes Ni atoms activated and accelerated break of O—H bond from H_2O and B—H bond from AB. Subsequently, the redox reactions separately proceed in the electron-rich metal and the hole-rich CNS. In this case, (1) M—H^- and M—H^+ will combine with each other to release hydrogen molecules (H^-H^+); (2) Two M—H^+ intermediates will also get two electrons from electron-rich Ni sites to form hydrogen molecules (H^+H^+); (3) Two M—H^- will also get two holes from hole-rich CNS sites at the interface between the metal and the CNS carrier to form hydrogen molecules

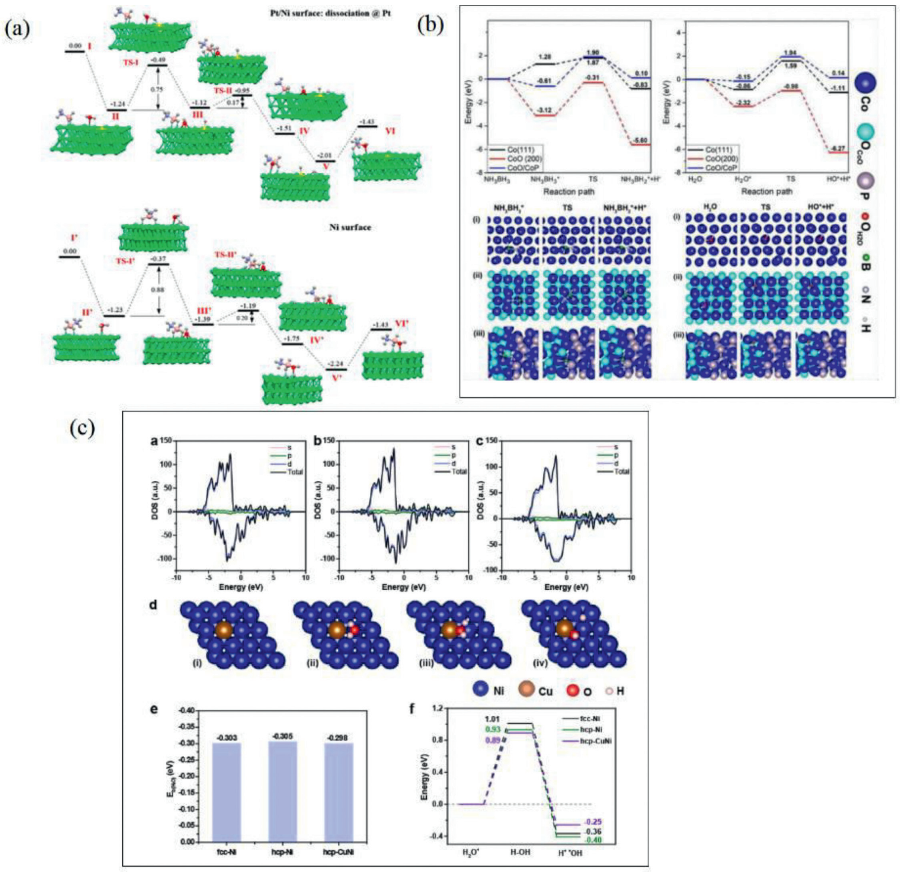

Fig. 8. (a) Simulated pathways of hydrolytic dehydrogenation of AB at Pt centre on atomic Pt substituted Ni surface (top) and at Ni centre on pristine Ni surface (bottom). Copied with permission [29]. Copyright 2017, American Chemical Society. (b) Energy profiles of AB and H_2O molecules dissociated on Co(111), CoO(200), and CoO/CoP surfaces. Copied with permission [34]. Copyright 2021, Elsevier. (c) Dissociation process and energy changes of H_2O molecules on fcc-Ni(111), hcp-Ni(0001), and hcp-CuNi(0001) model surfaces. Copied with permission [39]. Copyright 2022, Elsevier.

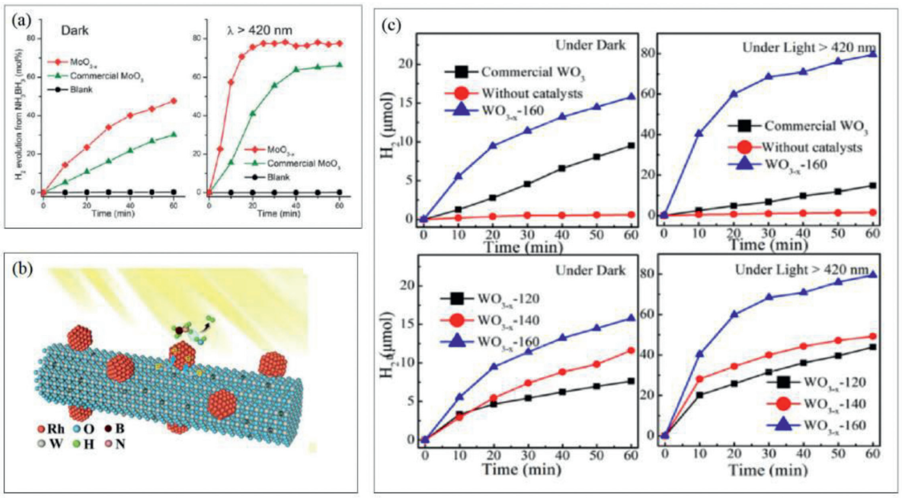

Fig. 9. (a) Time course of H_2 evolution from NH_3BH_3 aqueous solution at room temperature for different samples: in the dark and under visible light irradiation ($\lambda > 420$ nm). Copied with permission [95]. Copyright 2014, Wiley. (b) Structure model of Rh/WO_{3-x} hybrid nanowire catalysts. Copied with permission [98]. Copyright 2019, Royal Society of Chemistry. (c) H_2 evolution rate from ammonia borane over different catalysts: comparison of no catalyst, commercial WO_3 and WO_{3-x}-160 in dark and under light irradiation; comparison between WO_{3-x} and WO_{3-x}-120 in dark and under light irradiation. Copied with permission [97]. Copyright 2015, Wiley.

(H^-H^-). These intermediates $M{-}BH_2{}^+NH_3$ react with the $M{-}OH^-$ forming a H_3NBH_2OH species. Eventually, one molecule of AB and two molecules of H_2O produce three H_2 molecules and one molecule of NH_4BO_2 (Figs. 14b and c).

Whether single metal or binary metal clusters are attached to g-C_3N_4 surface (Cu/CNS, Ni/CNS and $Cu_{0.5}Ni_{0.5}$/CNS) [118], the band gap is greatly reduced and the transfer of photogenerated electrons and holes is increased, thus improving the photocatalytic activity. The calculated bandgap of pure CNS, Cu/CNS, Ni/CNS and $Cu_{0.5}Ni_{0.5}$/CNS were 1.18, 0.74, 0.54 and 0.36 eV respectively. β-SiC exhibits high catalytic activity when loaded with Pt and Ru clusters. By comparing the band structure of Pt/β-SiC and Ru/β-SiC

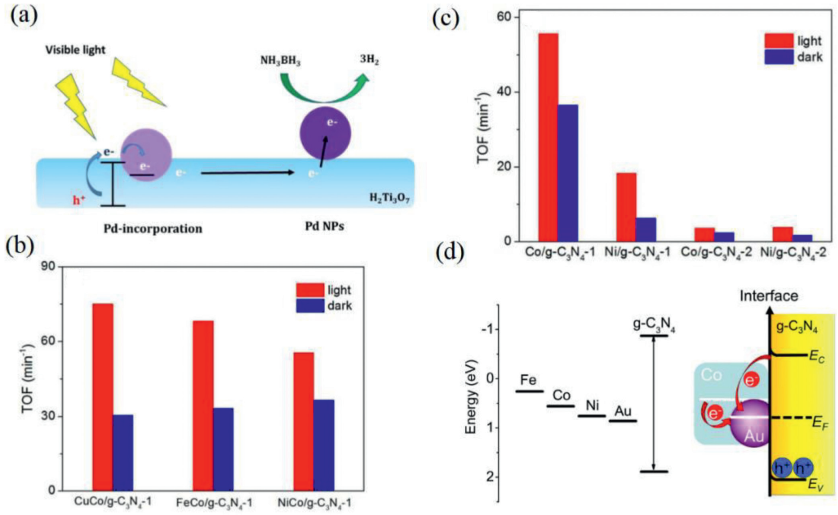

Fig. 10. (a) Schematic of the proposed mechanism for the hydrolysis of ammonia borane on Pd/$H_2Ti_3O_7$ composite nanowires. Copied with permission [99]. Copyright 2015, Elsevier. Comparison of TOF between (b) CoM/g-C_3N_4 (M = Cu, Fe, Ni) and (c) M/g-C_3N_4 (M = Co, Ni) catalysts. Copied with permission [100]. Copyright 2016, Royal Society of Chemistry. (d) Schematic view of Mott-Schottky type contact based on Au-Co hybrid nanoparticles. Copied with permission [101]. Copyright 2014, American Chemical Society.

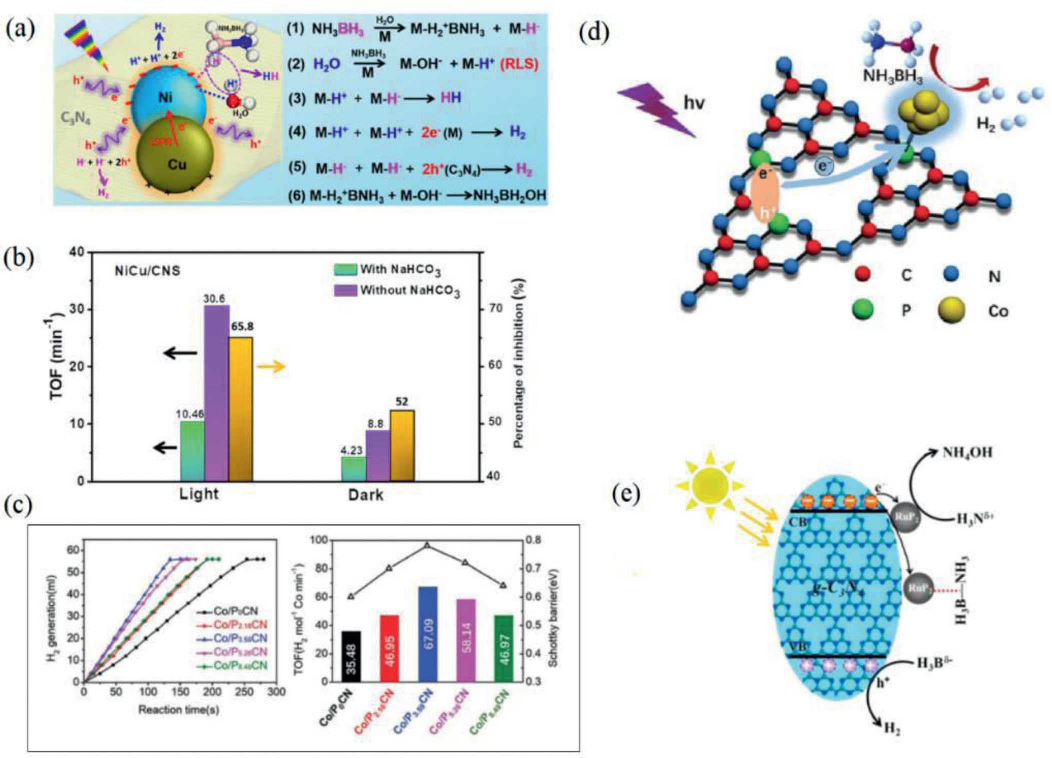

Fig. 11. (a) The plausible mechanism of ammonia borane hydrolysis on NiCu/CNS. Copied with permission [106]. Copyright 2020, American Chemical Society. (b) Activity comparison in the dark and under visible light irradiation with or without $NaHCO_3$ as a hole scavenger over NiCu/CNS. Copied with permission [106]. Copyright 2020, American Chemical Society. (c) Hydrogen evolution curves and TOF for the AB hydrolysis catalyzed by Co/P_0CN, Co/$P_{2.16}$CN, Co/$P_{3.59}$CN, Co/$P_{5.26}$CN, and Co/$P_{8.49}$CN under visible-light irradiation ([AB] = 170 mmol/L, 5 mL, $n_{Co}/n_{AB} = 0.02$, and $T = 298$ K). Copied with permission [107]. Copyright 2021, The Royal Society of Chemistry. (d) Structural model of Co/PCN catalyst. Copied with permission [107]. Copyright 2021, The Royal Society of Chemistry. (e) Schematic of the photocatalytic hydrolysis mechanism of AB using the prepared RP_2/CN. Copied with permission [109]. Copyright 2020, Elsevier.

with β-SiC [119]. Pure β-SiC is a wide band gap semiconductor catalyst, and the band gap of the Pt/β-SiC and Ru/β-SiC are less than the pure β-SiC. This is in good agreement with the experimental results (Fig. 15).

6. Effect of electric field

The electric field affects the distribution and transfer of charge, which is an important factor in catalytic reactions. A built-in elec-

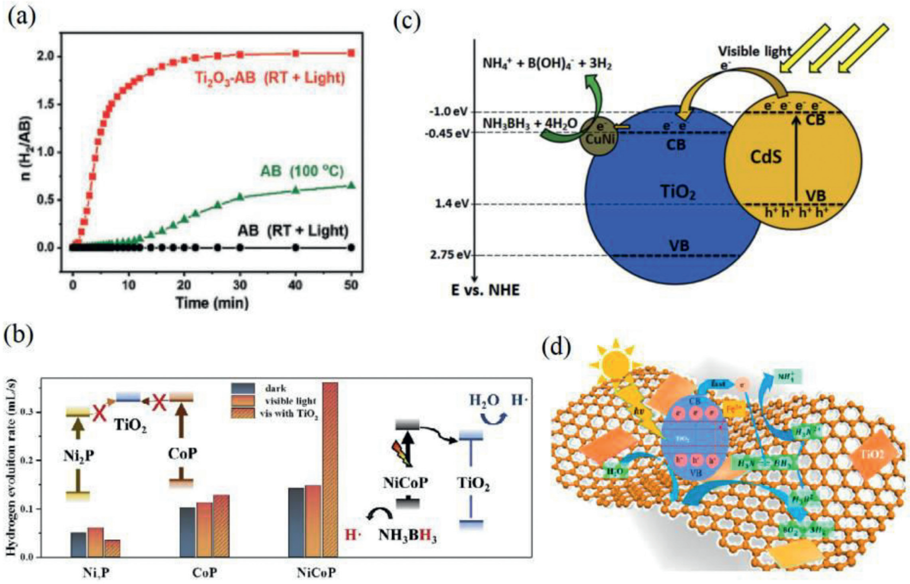

Fig. 12. (a) Hydrogen release from AB under different photothermal and thermal reaction conditions, with or without Ti_2O_3 photothermal materials (RT: room temperature). Copied with permission [111]. Copyright 2020, Wiley-VCH GmbH. (b) Schematic diagram of AB hydrolysis catalyzed by NiCoP nanostructure. Copied with permission [112]. Copyright 2019, Elsevier. (c) Schematic diagram of charge separation and transfer in the $Cu_{0.45}Ni_{0.55}/TiO_2CdS$ NTs system under visible-light irradiation. Copied with permission [113]. Copyright 2019, Elsevier. (d) Photocatalytic hydrolysis of ammonia borane to produce hydrogen. Copied with permission [114]. Copyright 2021, American Chemical Society.

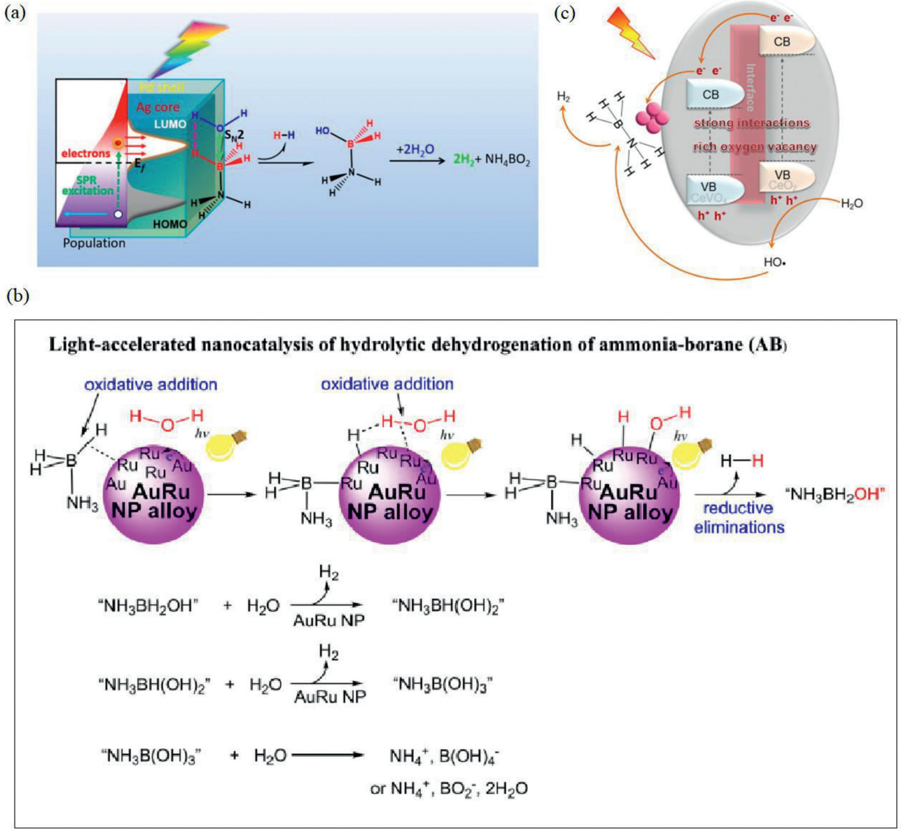

Fig. 13. (a) Proposed mechanism for the enhanced catalytic activity of Ag@Pd core-shell catalyst for AB hydrolysis under light illumination. Copied with permission [116]. Copyright 2020, American Chemical Society. (b) Mechanism for the visible-light-accelerated hydrolytic dehydrogenation of AB nanocatalyzed by Au_1Ru_1@Dendrimer1. Copied with permission [115]. Copyright 2020, American Chemical Society. (c) Possible mechanism for the H_2 production from an aqueous NH_3BH_3 solution over Co-$CeVO_4$/CeO_2 strong electronic interactions and rich oxygen vacancies under visible-light irradiation. Copied with permission [117]. Copyright 2021, American Chemical Society.

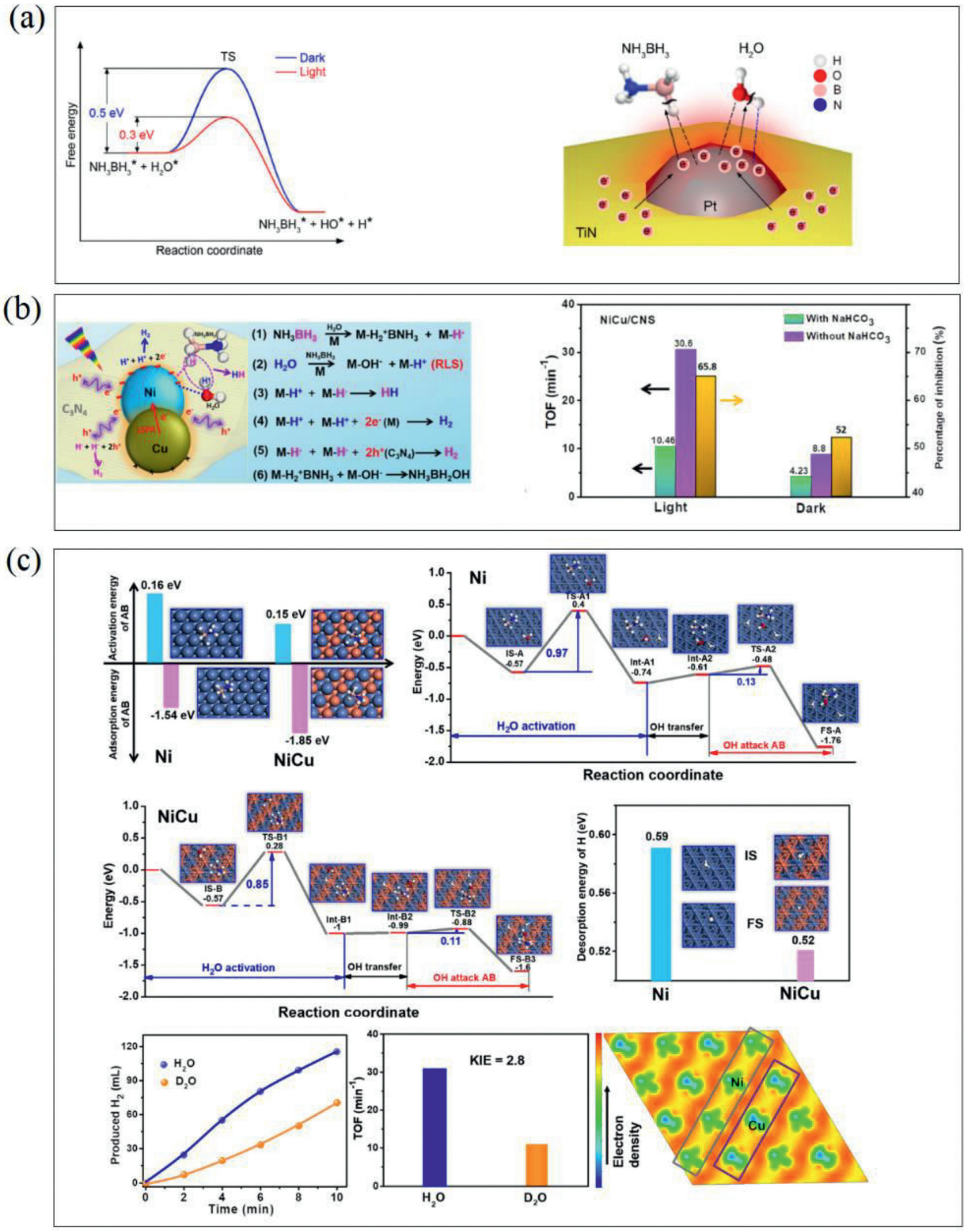

Fig. 14. (a) Schematic representation of the free energy plots showing the energy barriers associated with the formation of the reaction transition state (TS) of the RDS during NH_3BH_3 dehydrogenation reaction under light and dark conditions. Copied with permission [48]. Copyright 2020, American Chemical Society. (b) The plausible mechanism of ammonia borane hydrolysis on NiCu/CNS and activity comparison in the dark and under visible light irradiation with or without $NaHCO_3$ as a hole scavenger over NiCu/CNS. Copied with permission [106]. Copyright 2020, American Chemical Society. (c) Ni (Ni_{64}, gray blue) and NiCu (Cu: brown, $Ni_{32}Cu_{32}$) catalyzed AB hydrolysis and energy change. Copied with permission [106]. Copyright 2020, American Chemical Society.

tric field was formed on the surface of PtNi Alloy nanoparticles on Al_2O_3 (Al_2O_3-PtNi) catalyst, which promoted the process of AB dehydrogenation. As shown in Fig. 16a, the flow direction of electrons promotes the fracture of B-H bond and N-H bond, respectively [120].

With the help of the First-principles calculation simulation, activation of B-H bond in AB was achieved on BC_3 surface [121] by applied axial electric field (Fig. 16b). The applied electric field can act as a switch for the activation of B-H and N-H bonds in AB, and the dehydrogenation of AB can be realized under the action of the applied axial electric field. For Pt-M /BC_3N_2 (M = Al, Zn, Hf, Y) diatomic catalysts, B-H bond and N-H bond break process have different switching electric field (Fig. 16c) [122].

7. Photo-piezoelectric synergy catalysis

Photopiezoelectric co-catalysis has been widely used in dye degradation and water splitting [123–128]. The photo-piezoelectric synergy effect can improve catalytic activity, and since the dehydrogenation of AB involves both oxidation and reduction, the separation of electrons and holes becomes critical. In Ag_2O-$BaTiO_3$ hybrid photocatalyst, the built-in electric field is formed through continuous ultrasonic excitation to continuously separate photocarriers and improve the catalytic activity [129]. In the case of NIPS compounds (Ni_2P, $Ni_{12}P_5$ and Ni_3P) [130], illumination promotes electron-hole separation and migration to two different surfaces to

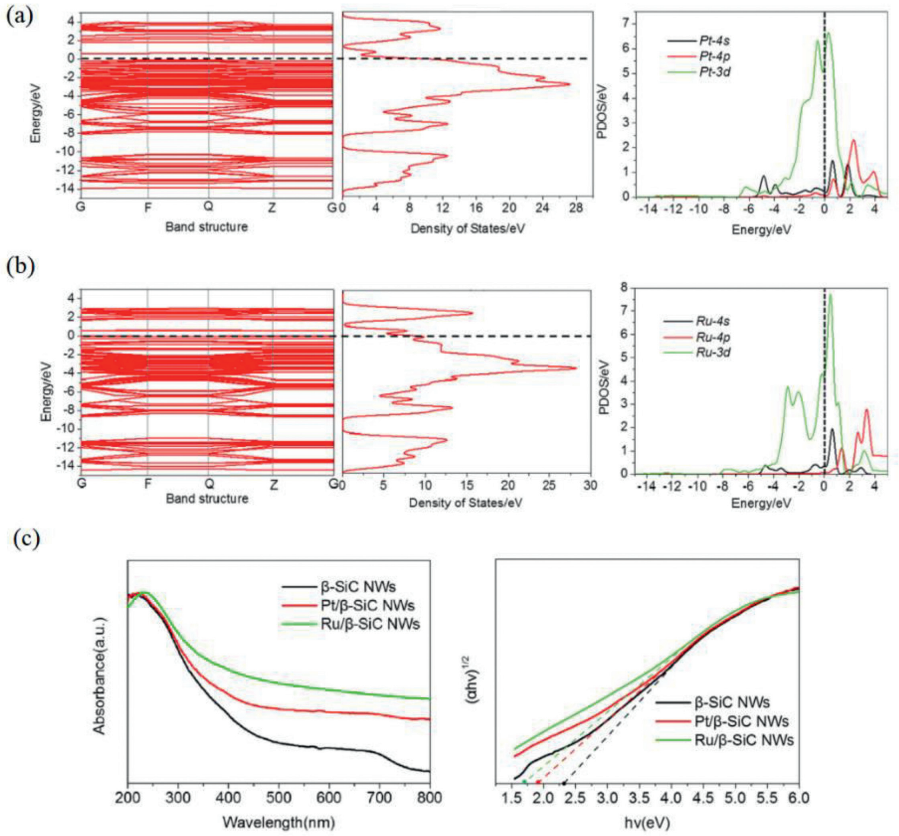

Fig. 15. Band structure, total density of states (TDOS), projected density of states (PDOS) of Pt/β-SiC and Ru/β-SiC. (a) Pt/β-SiC, (b) Ru/β-SiC. (c) UV-vis diffuses reflectance spectra and band-gap calculation of β-SiC, Pt/β-SiC, and Ru/β-SiC composite nanowires. Copied with permission [119]. Copyright 2019, Elsevier.

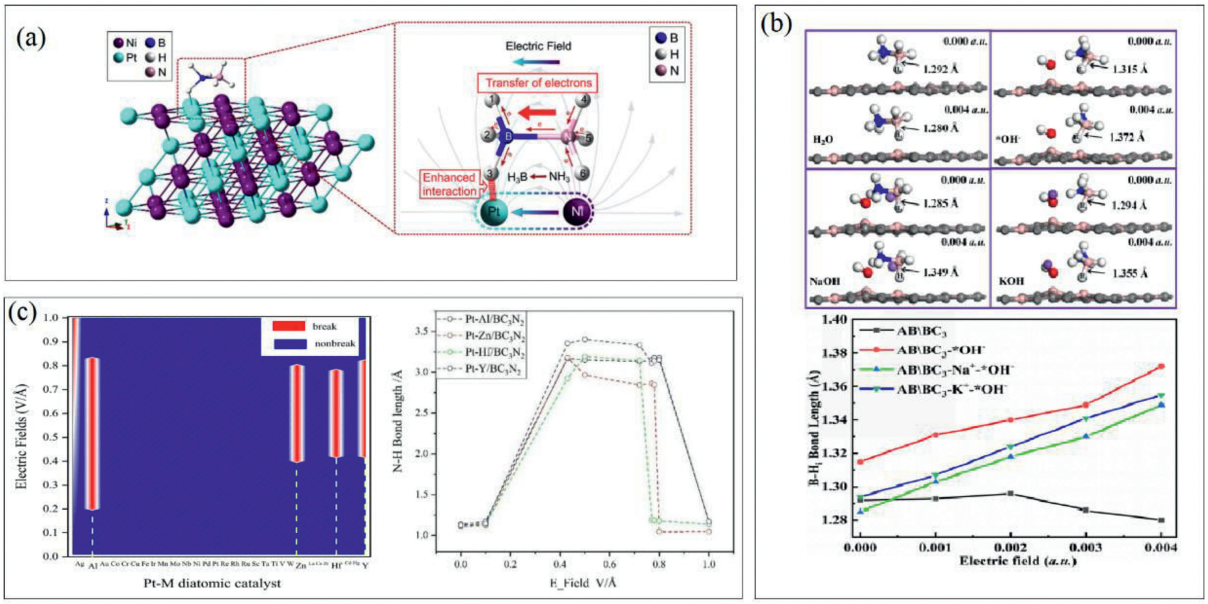

Fig. 16. (a) The adsorption configuration of AB molecule on PtNi (111) surface and the proposed mechanism for the effect of Pt-Ni dipole on the hydrolysis of AB. Copied with permission [120]. Copyright 2020, Elsevier. (b) Under the action of applied electric field, the negative and cationic loaded BC_3 catalyzes AB activation process. Copied with permission [121]. Copyright 2021, Elsevier. (c) The state of N-H bond in AB under different electric field (E_Field) on Pt-M/BC_3N_2 diatomic catalyst structure. Copied with permission [122]. Copyright 2022, Elsevier.

form oxidation and reduction active sites, respectively, catalyzing the dehydrogenation of AB.

MoS_2 is superior piezocatalyst and Doped with metal atoms could changes the band gap of MoS_2, allowing MoS_2 to be activated by visible light to generate electron-hole pairs (Fig. 17) [131]. Co-doped [132] and Sr-doped [133] MoS_2 two-dimensional materials can simultaneously form oxidation and reduction catalytic sites by forming a built-in electric field to promote electron-hole sep-

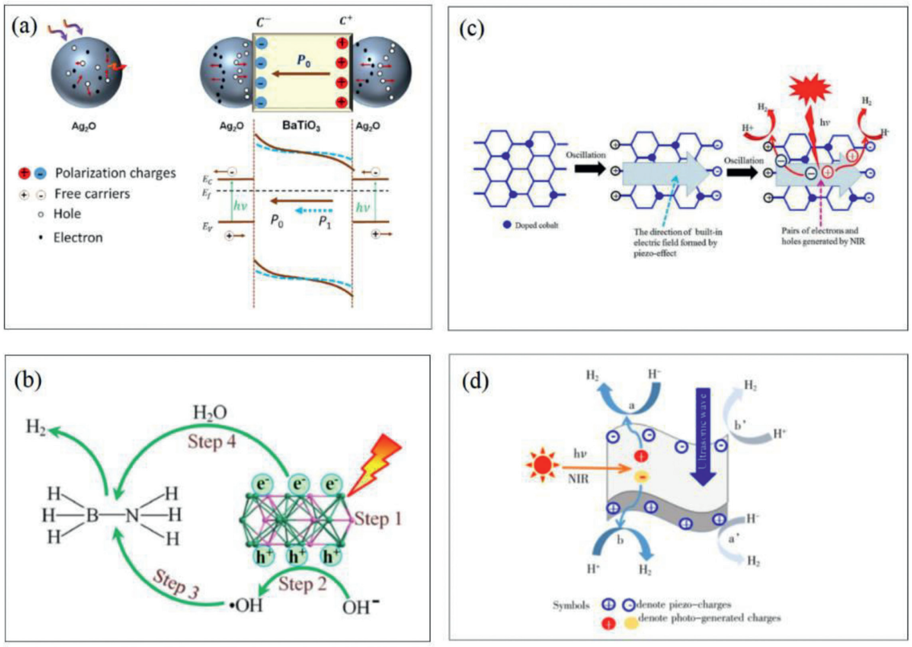

Fig. 17. (a) Schematic illustration of charge carrier generation in a Ag_2O nanoparticle when excited by a photon. (b) The separation of electrons and holes in Ag_2O nanoparticles attached to the two opposite surfaces of a $BaTiO_3$ nanocube that have opposite polarization charges due to piezoelectric effect and the corresponding tilting in the bands. Copied with permission [129]. Copyright 2015, American Chemical Society. (b) Possible mechanism for the hydrogen evolution from NH_3BH_3 in the alkaline aqueous solution over nickel phosphides under visible light irradiation. Copied with permission [130]. Copyright 2020, Wiley. (c) Reaction mechanism of piezo-photocatalytic H_2 production of Co-doped MoS_2. Copied with permission [132]. Copyright 2020, Royal Society of Chemistry. (d) Mechanism of hydrogen release from NH_3BH_3 solution by piezoelectric catalysis and piezo-enhanced NIR photocatalysis. Copied with permission [133]. Copyright 2021, China Academic Journal Electronic Publishing House.

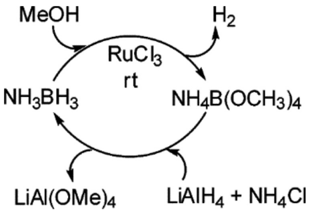

Fig. 18. Ammonia-borane hydrogen cycle. Copied with permission [69]. Copyright 2007, American Chemical Society.

aration under the photo-piezoelectric co-catalytic action, and can catalyze the break of B-H bond and N-H bond in AB to generate H_2 in the visible region.

8. Regeneration of AB

AB regeneration is an important part of AB dehydrogenation reaction, which determines the promotion of application scope of AB dehydrogenation reaction. Up to now, AB regeneration and recycling are realized by means of intermediates and alcohols [69,72,134]. AB was regenerated from methanolysis intermediate by following borate → $B(OH)_3$ → $B(OMe)_3$ → $NaBH_4$ → NH_3BH_3 (Fig. 18). The cost of regeneration is lower, and more environmentally friendly. And it could realize high yields (≥95%) and very high purity (≥98%).

Whether thermolysis, hydrolysis or methanolysis, AB can be regenerated by reaction byproducts. Sutton *et al.* [135] showed that the byproduct "BNH" after thermal decomposition of ammoniborane could react with N_2H_4 to regenerate BH_3NH_3 and realize the reaction cycle. Because the by-products of hydrolysis and alcoholysis have B-O bonds (NH_4BO_2 and $NH_4B(OCH_3)_4$), and B-O bonds are more stable than B-N bonds, it is more difficult to prepare BH_3NH_3 from the byproducts of hydrolysis and alcoholysis than from the products of thermal decomposition. Hausdorf *et al.* showed that AB can be recycled from the by-product of "BNH" and the reaction material can be saved as much as possible [136]. Through the byproduct of thermal decomposition reaction "BNH" to achieve AB regeneration, the reaction process is further simplified as [135]:

$$B_3N_3H_6 + 3N_2H_4 \rightarrow 3BH_3NH_3 + 3N_2\uparrow \tag{19}$$

AB can been regenerated by NH_4BO_2, a byproduct of the hydrolysis reaction, and the reaction process is as follows [137]:

$$BO_2^- + H^+ + H_2O \rightarrow H_3BO_3 \tag{20}$$

$$H_3BO_3 + 3CH_3OH \rightarrow B(OCH_3)_3 + 3H_2O \tag{21}$$

$$B(OCH_3)_3 + NH_4Cl + LiAlH_4 \rightarrow NH_3BH_3 + Al(OCH_3)_3 + LiCl + H_2 \tag{22}$$

Also, for methanolysis, AB can been regenerated by $NH_4B(OCH_3)_4$, a byproduct of the methanolysis reaction, and the reaction process is as follows [69]:

$$\begin{aligned} NH_4B(OCH_3)_4 + NH_4Cl + LiAlH_4 &\xrightarrow{\substack{\text{THF}\\ 9^\circ\text{C to RC}\\ 3-8\,\text{h}}} NH_3BH_3 + Al(OCH_3)_3 \\ &+ CH_3OH + H_2 + LiCl + NH_3 + H_2 + LiCl + NH_3 \end{aligned} \tag{23}$$

9. Summary and prospect

The high hydrogen capacity of 19.6 wt% has made AB an attractive material for chemical hydrogen storage. In this paper, we describe AB dehydrogenation from the aspects of thermal decomposition, hydrolysis, methanolysis, photocatalysis and photo-piezoelectric synergy catalyzes. The adaptive relationship between different catalyst structures and catalytic reaction types was explored, which provided important theoretical support for the design of AB dehydrogenation catalyst. The convenient generation and transportation of H_2 will expand the application scenarios of hydrogen energy and make important contributions to solving the energy crisis and environmental protection.

Declaration of competing interest

The authors declare that they have no known competing financial interests or personal relationships that could have appeared to influence the work reported in this paper.

Acknowledgments

This study were funded by the Natural Science Basic Research Program of Shaanxi (Nos. 2022JQ-108 and 2022JQ-096) and the National Natural Science Foundation of China (No. 22104079).

References

[1] Q. Li, Y. Wang, J. Zeng, et al., Chin. Chem. Lett. 32 (2021) 3355–3358.
[2] Y. Liu, Q. Feng, W. Liu, et al., Nano Energy 81 (2021) 105641.
[3] L. Chen, Y. Wang, X. Zhao, et al., J. Mater. Sci. Technol. 110 (2022) 128–135.
[4] S.G. Shore, R.W. Parry, J. Am. Chem. Soc. 77 (1955) 19–20.
[5] S.G. Shore, R.W. Parry, J. Am. Chem. Soc. 80 (1958) 8–12.
[6] D.J. Heldebrant, A. Karkamkar, J.C. Linehan, et al., Energy Environ. Sci. 1 (2008) 156.
[7] P.V. Ramachandran, B.C. Raju, P.D. Gagare, Org. Lett. 14 (2012) 6119–6121.
[8] P.V. Ramachandran, H. Mistry, A.S. Kulkarni, et al., Dalton Trans. 43 (2014) 16580–16583.
[9] P.V. Ramachandran, A.S. Kulkarni, Inorg. Chem. 54 (2015) 5618–5620.
[10] H.T. Hwang, A. Al-Kukhun, A. Varma, Int. J. Hydrog. Energy 37 (2012) 2407–2411.
[11] H.T. Hwang, A. Al-Kukhun, A. Varma, Int. J. Hydrog. Energy 37 (2012) 6764–6770.
[12] N. Patel, A. Kale, A. Miotello, Appl. Catal. B 111-112 (2012) 178–184.
[13] A.C. Gangal, P. Kale, R. Edla, et al., Int. J. Hydrog. Energy 37 (2012) 6741–6748.
[14] J.F. Petit, U.B. Demirci, Inorg. Chem. 58 (2019) 489–494.
[15] G.J. Kim, S.G. Hunt, H.T. Hwang, Int. J. Hydrog. Energy 45 (2020) 33751–33758.
[16] F. Toche, R. Chiriac, U.B. Demirci, et al., Int. J. Hydrog. Energy 37 (2012) 6749–6755.
[17] D. Salinas-Torres, M. Navlani-García, Y. Kuwahara, et al., Catal. Today 351 (2020) 6–11.
[18] M. Tong, Z. Yin, Y. Wang, et al., Int. J. Hydrog. Energy 38 (2013) 15285–15294.
[19] T. Zhou, G. Wang, H. Cui, et al., Int. J. Hydrog. Energy 41 (2016) 11746–11760.
[20] A. Kuang, T. Zhou, G. Wang, et al., Appl. Surf. Sci. 362 (2016) 562–571.
[21] H. Wu, Q.Q. Luo, R.Q. Zhang, et al., Chin. J. Chem. Phys. 31 (2018) 641–648.
[22] A.C. Gangal, P. Sharma, Int. J. Chem. Kinet. 45 (2013) 452–461.
[23] Q. Zhang, C. He, J. Huo, Comp. Mater. Sci. 207 (2022) 111306.
[24] C. He, Q. Zhang, J. Huo, et al., Chin. Chem. Lett. 33 (2022) 3281–3286.
[25] J. Huo, L. Fu, C. Zhao, et al., Chin. Chem. Lett. 32 (2021) 2269–2273.
[26] J. Huo, H. Wei, L. Fu, et al., Chin. Chem. Lett. 34 (2023) 107261.
[27] C.Y. Peng, L. Kang, S. Cao, et al., Angew. Chem. 127 (2015) 15951–15955.
[28] C. Hou, Q. Li, C. Wang, et al., Energy Environ. Sci. 10 (2017) 1770–1776.
[29] Z. Li, T. He, D. Matsumura, et al., ACS Catal. 7 (2017) 6762–6769.
[30] Q. Wang, F. Fu, S. Yang, et al., ACS Catal. 9 (2019) 1110–1119.
[31] Y. Peng, Y. He, Y. Wang, et al., J. Colloid Interface Sci. 594 (2021) 131–140.
[32] L. Semiz, Chem. Phys. Lett. 767 (2021) 138365.
[33] W. Wang, M. Liang, Y. Jiang, et al., Mater. Lett. 293 (2021) 129702.
[34] H. Wu, Y. Cheng, B. Wang, et al., J. Energy Chem. 57 (2021) 198–205.
[35] J. Xu, K. Feng, Y. Chen, et al., Appl. Surf. Sci. 537 (2021) 147823.
[36] J. Zhang, J. Li, L. Yang, et al., Int. J. Hydrog. Energy 46 (2021) 3964–3973.
[37] L. Zhao, Q. Wei, L. Zhang, et al., Renew. Energy 173 (2021) 273–282.
[38] Y. Chen, K. Feng, G. Yuan, et al., Chem. Eng. J. 428 (2022) 131219.
[39] P. Li, R. Chen, Y. Huang, et al., Appl. Catal. B 300 (2022) 120725.
[40] H. Song, Y. Cheng, B. Li, et al., ACS Sustain. Chem. Eng. 8 (2020) 3995–4002.
[41] Y. SÜRME, Int. J. Chem. Technol. 4 (2020) 103–108.
[42] S. Akbayrak, S. Ozkar, J. Colloid Interface Sci. 596 (2021) 100–107.
[43] Y. Feng, Y. Shao, X. Chen, et al., ACS Appl. Energy Mater. 4 (2021) 633–642.
[44] Y. He, Y. Peng, Y. Wang, et al., Fuel 297 (2021) 120750.
[45] X. Huang, Y. Liu, H. Wen, et al., Appl. Catal. B 287 (2021) 119960.
[46] J. Liu, P. Li, R. Jiang, et al., ChemCatChem 13 (2021) 1–10.
[47] H. Lv, R. Wei, X. Guo, et al., J. Phys. Chem. Lett. 12 (2021) 696–703.
[48] S. Rej, L. Mascaretti, E.Y. Santiago, et al., ACS Catal. 10 (2020) 5261–5271.
[49] Q. Xu, M. Chandra, J. Power Sources 163 (2006) 364–370.
[50] D. Sun, V. Mazumder, O. Metin, et al., ACS Nano 5 (2011) 6458–6464.
[51] Z.C. Fu, Y. Xu, S.L. Chan, et al., Chem. Commun. 53 (2017) 705–708 Camb..
[52] C. Tang, F. Qu, A.M. Asiri, et al., Inorg. Chem. Front. 4 (2017) 659–662.
[53] B. Coşkuner Filiz, A. Kantürk Figen, P. Sabriye, Appl. Catal. A: Gen. 550 (2018) 320–330.
[54] F. Fu, C. Wang, Q. Wang, et al., J. Am. Chem. Soc. 140 (2018) 10034–10042.
[55] Q. Zhou, L. Qi, H. Yang, et al., J. Colloid Interface Sci. 513 (2018) 258–265.
[56] Y. Lin, L. Yang, H. Jiang, et al., J. Phys. Chem. Lett. 10 (2019) 1048–1054.
[57] Y. Wang, D. Wang, C. Zhao, et al., Int. J. Hydrog. Energy 44 (2019) 10508–10518.
[58] X. Yang, Q. Li, L. Li, et al., J. Power Sources 431 (2019) 135–143.
[59] M. Zhang, X. Xiao, Y. Wu, et al., Catalysts 9 (2019) 1009.
[60] X. Zhou, X.F. Meng, J.M. Wang, et al., Int. J. Hydrog. Energy 44 (2019) 4764–4770.
[61] S. Akbayrak, Y. Tonbul, S. Özkar, ACS Sustain. Chem. Eng. 8 (2020) 4216–4224.
[62] W. Chen, W. Fu, G. Qian, et al., iScience 23 (2020) 100922.
[63] L.L. Fu, D.F. Zhang, Z. Yang, et al., ACS Sustain. Chem. Eng. 8 (2020) 3734–3742.
[64] Y.T. Li, X.L. Zhang, Z.K. Peng, et al., Fuel 277 (2020) 118243.
[65] Y.T. Li, X.L. Zhang, Z.K. Peng, et al., ACS Sustain. Chem. Eng. 8 (2020) 8458–8468.
[66] S. Prabu, K.Y. Chiang, Mater. Adv. 1 (2020) 1952–1962.
[67] M. Rakap, Renew. Energy 154 (2020) 1076–1082.
[68] J. Li, Q. Guan, H. Wu, et al., J. Am. Chem. Soc. 141 (2019) 14515–14519.
[69] P.V. Ramachandran, P.D. Gagare, Inorg. Chem. 46 (2007) 7810–7817.
[70] Y. Karataş, M. Gülcan, M. Çelebi, et al., ChemistrySelect 2 (2017) 9628–9635.
[71] C. Reller, F.O. Mertens, Angew. Chem. Int. Ed. 51 (2012) 11731–11735.
[72] C. Reller, F. Mertens, ChemPlusChem 83 (2018) 1013–1020.
[73] H. Erdogan, O. Metin, S. Ozkar, Phys. Chem. Chem. Phys. 11 (2009) 10519–10525.
[74] D. Sun, V. Mazumder, Ö. Metin, et al., ACS Catal. 2 (2012) 1290–1295.
[75] D. Sun, P. Li, B. Yang, et al., RSC Adv. 6 (2016) 105940–105947.
[76] P. Lara, K. Philippot, A. Suárez, ChemCatChem 11 (2019) 766–771.
[77] H.B. Dai, X.D. Kang, P. Wang, Int. J. Hydrog. Energy 35 (2010) 10317–10323.
[78] Y. Karatas, M. Gülcan, F. Sen, Int. J. Hydrog. Energy 44 (2019) 13432–13442.
[79] H. Erdoğan, Ö. Metin, S. Özkar, Catal. Today 170 (2011) 93–98.
[80] S. Peng, J. Liu, J. Zhang, et al., Int. J. Hydrog. Energy 40 (2015) 10856–10866.
[81] Y. Fang, J. Li, T. Togo, et al., Chem 4 (2018) 555–563.
[82] S. Çalışkan, M. Zahmakıran, S. Özkar, Appl. Catal. B 93 (2010) 387–394.
[83] D. Özhava, S. Özkar, Appl. Catal. B 237 (2018) 1012–1020.
[84] W. Luo, W. Cheng, M. Hu, et al., ChemSusChem 12 (2019) 535–541.
[85] B. Abay, M. Rakap, Catal. Sci. Technol. 10 (2020) 7270–7279.
[86] D. Özhava, S. Özkar, Int. J. Hydrog. Energy 40 (2015) 10491–10501.
[87] D. Özhava, S. Özkar, Appl. Catal. B 181 (2016) 716–726.
[88] D. Özhava, S. Özkar, Mol. Catal. 439 (2017) 50–59.
[89] J.K. Sun, W.W. Zhan, T. Akita, et al., J. Am. Chem. Soc. 137 (2015) 7063–7066.
[90] Q. Yao, M. Huang, Z.H. Lu, et al., Dalton Trans. 44 (2015) 1070–1076.
[91] M. Yurderi, A. Bulut, İ.E. Ertas, et al., Appl. Catal. B 165 (2015) 169–175.
[92] C. Yu, J. Fu, M. Muzzio, et al., Chem. Mater. 29 (2017) 1413–1418.
[93] K. Mori, P. Verma, R. Hayashi, et al., Chemistry 21 (2015) 11885–11893.
[94] S. Jo, P. Verma, Y. Kuwahara, et al., J. Mater. Chem. A 5 (2017) 21883–21892.
[95] H. Cheng, T. Kamegawa, K. Mori, et al., Angew. Chem. Int. Ed. 53 (2014) 2910–2914.
[96] H. Yin, Y. Kuwahara, K. Mori, et al., J. Mater. Chem. A 5 (2017) 8946–8953.
[97] Z. Lou, Q. Gu, L. Xu, et al., Chem. Asian J. 10 (2015) 1291–1294.
[98] X. Li, Y. Yan, Y. Jiang, et al., Nanoscale Adv. 1 (2019) 3941–3947.
[99] S.W. Lai, J.W. Park, S.H. Yoo, et al., Int. J. Hydrog. Energy 41 (2016) 3428–3435.
[100] H. Zhang, X. Gu, P. Liu, et al., J. Mater. Chem. A 5 (2017) 2288–2296.
[101] L.T. Guo, Y.Y. Cai, J.M. Ge, et al., ACS Catal. 5 (2014) 388–392.
[102] B. Pant, H.R. Pant, M. Park, et al., Catal. Commun. 50 (2014) 63–68.
[103] M. Wen, Y. Cui, Y. Kuwahara, et al., ACS Appl. Mater. Interfaces 8 (2016) 21278–21284.
[104] H. Zhang, X. Gu, J. Song, et al., ACS Appl. Mater. Interfaces 9 (2017) 32767–32774.
[105] J. Song, X. Gu, J. Cheng, et al., Appl. Catal. B 225 (2018) 424–432.
[106] S. Zhang, M. Li, L. Li, et al., ACS Catal. 10 (2020) 14903–14915.
[107] S.H. Xu, J.F. Wang, A. Valério, et al., Inorg. Chem. Front. 8 (2021) 48–58.
[108] M. Navlani-García, P. Verma, Y. Kuwahara, et al., J. Photochem. Photobiol. A Chem. 358 (2018) 327–333.
[109] L. Wei, Y. Yang, Y.N. Yu, et al., Int. J. Hydrog. Energy 46 (2021) 3811–3820.
[110] J. Song, X. Gu, Y. Cao, et al., J. Mater. Chem. A 7 (2019) 10543–10551.
[111] H. Huang, C. Wang, Q. Li, et al., Adv. Funct. Mater. 31 (2020) 2007591.
[112] Y. Wang, G. Shen, Y. Zhang, et al., Appl. Catal. B 260 (2020) 118183.
[113] D. Sun, Y. Hao, C. Wang, et al., Int. J. Hydrog. Energy 45 (2020) 4390–4402.
[114] Y. Yan, J. Li, T. Jia, et al., Energy Fuels 35 (2021) 16035–16045.
[115] N. Kang, Q. Wang, R. Djeda, et al., ACS Appl. Mater. Interfaces 12 (2020) 53816–53826.
[116] P. Xu, W. Lu, J. Zhang, et al., ACS Sustain. Chem. Eng. 8 (2020) 12366–12377.
[117] J. Song, F. Wu, Y. Lu, et al., ACS Appl. Nano Mater. 4 (2021) 4800–4809.
[118] R. Fang, Z. Yang, Z. Wang, et al., Energy 244 (2022) 123187.
[119] H. Li, Y. Yan, S. Feng, et al., Fuel 255 (2019) 115771.
[120] B. Wang, L. Xiong, H. Hao, et al., J. Alloys Compd. 844 (2020) 156253.
[121] J. Yu, C. He, J. Huo, et al., Int. J. Hydrog. Energy 47 (2022) 7738–7750.
[122] J. Huo, H. Wei, L. Fu, et al., Mater. Today. Commun. 31 (2022) 103544.
[123] D. Hong, W. Zang, X. Guo, et al., ACS Appl. Mater. Interfaces 8 (2016) 21302–21314.
[124] H. You, Z. Wu, Y. Jia, et al., Chemosphere 183 (2017) 528–535.
[125] S. Li, Z. Zhao, D. Yu, et al., Nano Energy 66 (2019) 104083.
[126] D. Yu, Z. Liu, J. Zhang, et al., Nano Energy 58 (2019) 695–705.
[127] K.S. Hong, H. Xu, H. Konishi, et al., J. Phys. Chem. Lett. 1 (2010) 997–1002.
[128] R. Tang, D. Gong, Y. Zhou, et al., Appl. Catal. B 303 (2022) 120929.

[129] H. Li, Y. Sang, S. Chang, et al., Nano Lett. 15 (2015) 2372–2379.
[130] J. Song, X. Gu, H. Zhang, ChemistryOpen 9 (2020) 366–373.
[131] M. Pan, S. Liu, J.W. Chew, Nano Energy 68 (2020) 104366.
[132] S. Liu, K. Huang, W. Liu, et al., New J. Chem. 44 (2020) 14291–14298.
[133] Zhou Yiwen, Huang Kuangzheng, Liu Wenxiao, et al., J. Suzhou Univ. Sci. Technol. 38 (2021) 1–11.
[134] S. Özkar, Int. J. Hydrog. Energy 45 (2020) 7881–7891.
[135] A.D. Sutton, A.K. Burrell, D.A. Dixon, et al., Science 331 (2011) 1426–1429.
[136] S. Hausdorf, F. Baitalow, G. Wolf, et al., Int. J. Hydrog. Energy 33 (2008) 608–614.
[137] Q. Yao, H. Du, Z.H. Lu, Prog. Chem. 32 (2020) 1930–1951.